Laura's Thesis oh yah

A Dissertation

Presented to

The Faculty of the Graduate School of Arts and Sciences

Brandeis University

Department of Physics

Professor Gabriella Sciolla, Advisor

In Partial Fulfillment

of the Requirements for the Degree

Doctor of Philosophy

by

Laura Bergsten

July, 2020

This dissertation, directed and approved by Laura Bergsten's committee, has been accepted and approved by the Graduate Faculty of Brandeis University in partial fulfillment of the requirements for the degree of:

DOCTOR OF PHILOSOPHY

Eric Chasalow, Dean of Arts and Sciences

Dissertation Committee:

Professor Gabriella Sciolla, Chair

Craig Blocker

Alessandro Tricoli

For my family

Acknowledgments

This is to thank all the people. Gabriella and committee. Gaetano and Alessandro. All group members. Friends and family for sanity.

Abstract

Laura's Thesis oh yah

A dissertation presented to the Faculty of
the Graduate School of Arts and Sciences of
Brandeis University, Waltham, Massachusetts

by Laura Bergsten

The Higgs boson is measured by me in a channel it is nice and I graduate call me doctor

Contents

Chapter 1

Introduction

Introduction to the thesis. Explain what u'll see.

Chapter 2

Theory

2.1 Standard Model

The Standard Model (SM) is the leading theory that describes interactions between particles at a subatomic scale. I begin with a brief summary of the SM itself beginning with brief descriptions of the fundamental particles and their forces before delving into a summarized mathematical formulation. Next, I discuss the history of the SM and crucial tests of the theory up until current work at the LHC. I will then outline some of the recent and current physics at the Large Hadron Collider (LHC) with a focus on Higgs boson measurements. Finally, I'll introduce my thesis' main focus, differential cross-section measurements of Vector-Boson-Fusion Higgs decaying into two W-bosons.

The Standard Model is one of the most successful scientific theories to date. Its predictions encompass all of the visible universe and continue to undergo careful testing. The SM combines three forces- electromagnetic, weak, and strong - into one elegant description. I'll follow in the steps of many before me and detail the theory through first introducing particles and forces. Next I will introduce the mathematical formalisms describing particle interactions.

2.1.1 Particles and forces

The particles we define in high energy physics are the most minute portions of matter we're able to observe. They are generally considered point-like, have no internal structure, and cannot be further split. Each particle we can define has a unique set of quantum numbers and its own anti-particle (with the same mass and spin, but opposite electrical charge and quantum numbers).

Particles can split up into distinct groups- first bosons, with integer spin, and fermions, with half-integer spin. Bosons are 'force carriers' meaning when particles interact they exchange bosons. Fermions are at the heart of all conventional matter. Fermions can be split further into two categories- leptons and quarks. Quarks have fractional integer charge and interact strongly while leptons have integer charge and interact solely through the weak or electromagnetic forces. Both quarks and leptons are made of three generations of particles, each heavier and more unstable than the next. Charts showing quark/lepton families and their key quantum numbers are shown below. Each generation of quarks and leptons contains a particle doublet. Each lepton doublet contains a charged lepton and a neutrino while each quark doublet contains one $+2/3$ charged particle and one with a $-1/3$ charge. Each lepton and quark also has an anti-particle. All conventional, stable matter is made from the first generation of quarks and leptons.

There are four gauge bosons and one scalar boson predicted through the SM. These correspond to three fundamental forces in nature (the fourth, gravity, is so small on the scale of particle interactions as to not be considered). The strongest force on the subatomic scale is the strong force- this is mediated by the gluon- and works primarly to bind quarks together to form composite particles like protons or neutrons. The electromagnetic force is about 60x weaker than the strong force and is mediated by the photon. This force accounts for all electric interactions like that between an electron an an atomic nucleus. Finally, the weak force (10^4 weaker than the EM) facilitates β-decay and is mediated by massive Z and W bosons. Before going into more detail on the gauge bosons and the forces they mediate, I'd be remiss not to mention the Higgs boson. The only scalar boson predicted by the SM, it is has no charge or intrinsic spin. The Higgs gives mass to all other particles through Spontaneous Symmetry Breaking, which I'll expand on in later sections.

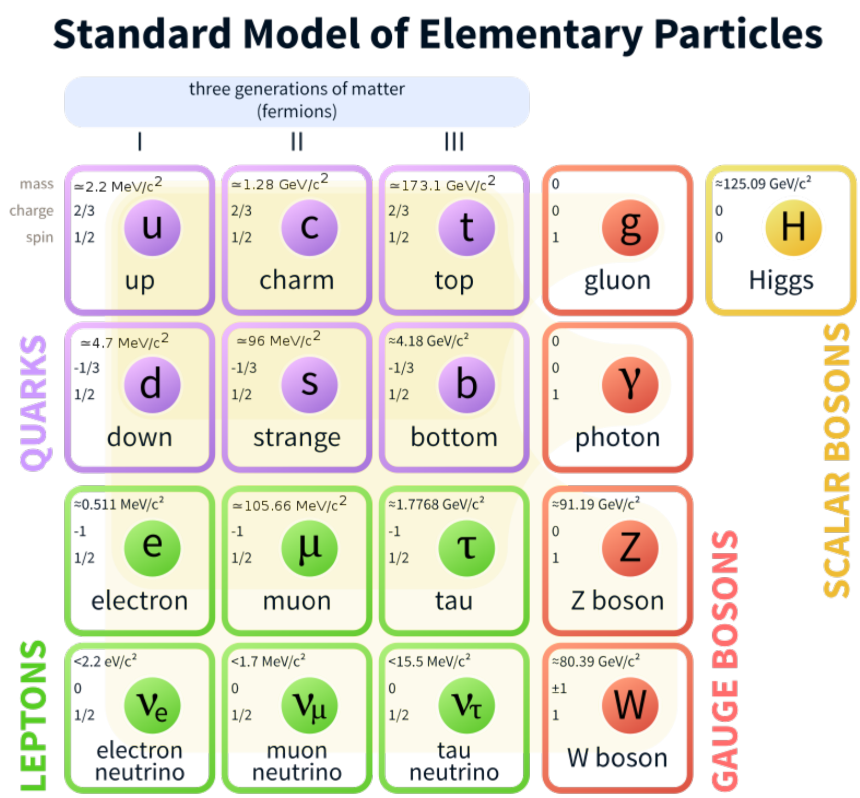

Figure 2.1: Three generations of quarks and leptons are shown along with all SM bosons (25)

Photons are massless, spin-1 particles and mediate all electromagnetic interactions. They couple directly to any particle with electric charge- so quarks, leptons, and W/Z bosons but not neutrinos. Since the photon is massless, the electromagnetic force can operate on infinitely long scales but it's force decreases with $1/r^2$.

Gluons are massless particles with no charge and a spin-1. They couple to color charges, which are a property of quarks. Each quark has one of three colors (RGB) while anti-quarks have "anti" versions of these. Colors ore conserved 'charges' just like electric charge. Quarks are never found alone as they couple so strongly to one another as to be confined in groups of two or three. These groups are "color-confined" meaning the quarks contain colors which add up to a color neutral sum. For instance, a two quark meson $u\bar{u}$ may have colors R and anti-R while a three quark hadron uud (proton) may have colors R, G, and B. Gluons are different from photons in that they are not neutral to the charge they couple to. Gluons have two colors (8 total combinations) and can thus couple to each other. This makes the strong force distinct from the electromagnetic and has implications for long-distance interactions.

W and Z bosons, unlike gluons and photons, are massive. However, like their other gauge boson counterparts, they have spin-1 and mediate a charge (weak). $W^{\pm}$ mediates charged-current interactions which can violate flavor conservation between quarks and/or leptons and their neutrinos. Z^0 mediates neutral-current interactions which conserve flavor. $W^{\pm}$ bosons contain electric charge so can interact through EM as well. In addition, W and Z bosons contain weak charge (as do all fermions) so can self-couple as well as couple with all fermions.

The Higgs boson will be further motivated and described in later sections but suffice to say it's a massive spin-0 particle which couples to all particles with mass (including itself). It doesn't mediate any force but is still an integral part of the SM.

2.1.2 Gauge Invariance

According to Noether's theorem, for every continuous transformation of a field that leaves the Lagrangian invariant, there is a conserved current. Symmetries found in physical theories lead to conservation laws (and vice-versa). The Standard Model is a gauge theory built on symmetries such that all interactions between particles result from requiring the theory to be invariant under local gauge transformations. Each part of the Standard Model- from quantum electrodynamics (QED) to quantum chromodynamics (QCD) - is a gauge theory on its own, which simply means they have gauge invariance symmetries. In this section I'll step through the basic mathematic formalism for QED, QCD, and the combined electroweak theory to illustrate the physical ramifications of gauge invariance and set the stage for the Higgs mechanism. The following sections are written with guidance from text (20).

Quantum Electrodynamics

Quantum electrodynamics (QED) is the first, and simplest, physical gauge theory, describing how light and matter interact even under relativistic conditions. The theory produces extremely good agreement with experiment due to the success of perturbative solutions and entire textbooks are dedicated to its motivation and calculated predictions. Here I will generate the full QED Lagrangian by imposing local gauge invariance on the Lagrangian of a free fermion.

First, the Dirac Lagrangian describes a free fermion of mass m

$$\mathcal{L} = i\psi\gamma^\mu\partial_\mu\psi - m\bar{\psi}\psi, \tag{2.1}$$

where ψ is a Dirac spinor and γ^μ represent the Dirac matrices. To demonstrate local gauge invariance we need to transform

$$\psi(x) \rightarrow e^{i\alpha(x)}\psi(x) \tag{2.2}$$

where $\alpha(x)$ depends on space and time arbitrarily. Directly substituting this into our Lagrangian shows that $\mathcal{L}$ is not invariant, and the ∂_μ term breaks this

$$\partial_\mu\psi \rightarrow e^{i\alpha(x)}\partial_\mu\psi + ie^{i\alpha(x)}\partial_\mu\alpha \tag{2.3}$$

In order to mandate the theory is invariant we need to change this term to the "covariant derivative" D_μ which transforms

$$D_\mu\psi \rightarrow e^{i\alpha(x)}D_\mu\psi. \tag{2.4}$$

In order to transform as such the "covariant derviative" has to contain a vector field A_μ and this field must transform so as to cancel with the unwanted part of the transformed D_μ.

$$D_\mu \equiv \partial_\mu - ieA_\mu \tag{2.5}$$

where

$$A_\mu \rightarrow A_\mu + \frac{1}{e}\partial_\mu\alpha \tag{2.6}$$

Now the original Dirac equation is replaced with the following:

$$\mathcal{L} = \bar{\psi}(i\gamma^\mu\partial_\mu - m)\psi + e\bar{\psi}\gamma^\mu\psi A_\mu. \tag{2.7}$$

By requiring local gauge invariance we've introduced a gauge field A_μ which couples to the Dirac particle just as the photon. In fact, if we take this as the photon gauge field and so add a kinetic energy term (which is also local gauge invariant!) we find the Lagrangian of

QED.

$$\mathcal{L} = \bar{\psi}(i\gamma^\mu \partial_\mu - m)\psi + e\bar{\psi}\gamma^\mu \psi A_\mu - \frac{1}{4}F_{\mu\nu}F^{\mu\nu} \tag{2.8}$$

One can also see that adding a mass term to the Lagrangian for the new field ($\frac{1}{2}m^2 A_\mu A^\mu$) would break gauge invariance, indicating the photon must be massless. From the free fermion Lagrangian, imposing local gauge invariance leads to the full interacting field theory of QED. This isn't a curiosity but an essential component of the theory, and the use of local gauge symmetry in deriving particle interactions doesn't end here.

Quantum chromodynamics

Quantum chromodynamics differs from QED in a few crucial ways. First, since quark color fields exist the QED $U(1)$ gauge group is replaced with $SU(3)$ and the free Lagrangian contains indices j to denote the three color fields.

$$\mathcal{L} = \bar{q}_j(i\gamma^\mu \partial_\mu - m)q_j. \tag{2.9}$$

QCD also carries three quark flavors, which will be ignored here for simplicity. The QCD group is also non-Abelian since not all generators of the group commute with each other. These generators will be defined as T_a where $= 1, ..., 8$ and are linearly independent traceless 3×3 matrices (the Gell-Mann matrices λ_a are conventional). The local color phase transformation required is thus

$$q(x) \rightarrow e^{i\alpha_a(x)T_a} q(x) \tag{2.10}$$

We can consider an infinitesimal phase transformation as

$$q(x) \rightarrow [1 + i\alpha_a(x)T_a]q(x), \partial_u q \rightarrow (1 + i\alpha_a T_a)\partial_\mu q + iT_a q \partial_\mu \alpha_a. \tag{2.11}$$

Just as in the QED example, the last line breaks the invariance of $\mathcal{L}$ and we can proceed very similarly to the QED case by introducing a new gauge field (or in this case eight) called G^a_μ which transform

$$G^a_\mu \rightarrow G^a_\mu - \frac{1}{g}\partial_\mu \alpha_a - f_{abc}\alpha_b G^c_\mu \tag{2.12}$$

The last term added here is to cope with the non-Abelian nature of QCD (that not all the generators T_a commute with each other). Just as in QED this invariance forms a covariant derviative

$$D_\mu = \partial_m u + igT_a G^a_\mu \tag{2.13}$$

Replacing the derivative into our Lagrangian and adding a gauge invariant energy term for each of the $G_m u^a$ fields ($\frac{1}{4}G^a_{\mu\nu}G^a_{\mu\nu}$) yields the final gauge invariant QCD Lagrangian

$$\mathcal{L} = \bar{q}(i\gamma^\mu \partial_\mu - m)q - g(\bar{q}\gamma^\mu T_a q)G^a_\mu - \frac{1}{4}G^a_{\mu\nu}G^a_{\mu\nu}. \tag{2.14}$$

Just as in the QED case, imposing local color phase invariance produced a new interacting field (or rather, eight) with a coupling specified as g. These are the gluon fields and just like photons, local gauge invariance requires them to be massless. Unlike the QED case, this Lagrangian's new kinetic term includes self-interaction between the gauge bosons - another key feature of QCD that is mandated by local color phase invariance. Gluons themselves must carry color charge and so self-couple - the structure of these self coupling terms and their single coupling strength g are uniqely determined by gauge invariance.

Electroweak unification

Thus far, I've summarized the theoretical backgrounds for symmetries (and so conserved quantities) in both quantum electrodynamics and chromodynamics. The weak force is the final Standard Model force and weak interactions are mediated by Z and W bosons. Unlike the gluons and photons of QCD and QED, these gauge bosons are massive. This is explained through spontaneous symmetry breaking of the electroweak force, which is descibed in the following section. Assuming that W/Z bosons are massive, the weak force can be combined with QED and a central electroweak force (with its associated symmetries) can be described.

The weak neutral current J_μ^{NC} as well as the charged currents J_μ and $J_\mu^\dagger$ can form a symmetry group of weak interactions. The charged currents correspond to the charged weak interaction with $W^\pm$ bosons while the neutral current is associated with the Z^0 boson.

$$J_\mu = \bar{\nu_L}\gamma_\mu\nu_L J_\mu^\dagger = \bar{e_L}\gamma_\mu\nu_L J_\mu^3 = \frac{1}{2}\bar{\nu_L}\gamma_\mu\nu_L - \frac{1}{2}\bar{e_L}\gamma_\mu e_L \tag{2.15}$$

L here denotes that these are left-handed spinors and particle names denote associated Dirac spinors. The charged currents can be written as a doublet using the Pauli spin matrices τ_i where $\tau_\pm = \frac{1}{2}(\tau_1 \pm i\tau_2$ and

$$\chi_L = \begin{bmatrix} \nu \\ e^- \end{bmatrix} \tag{2.16}$$

as

$$J_\mu^+(x) = \bar{\chi_L}\gamma_\mu\tau_+\chi_L J_\mu^+(x) = \bar{\chi_L}\gamma_\mu\tau_-\chi_L J_\mu^3(x) = \bar{\chi_L}\gamma_\mu\frac{1}{2}\tau_i\chi_L \text{with} i = 1,23 \tag{2.17}$$

Now if a corresponding charge is defined $T^i = \int J_0^i(x)d^3x$ we have an $SU(2)_L$ algebra

$$[T^i, T^j] = i\epsilon_{ijk}T^k \tag{2.18}$$

Unfortunately while a these currents create an $SU(2)$ group, they don't correspond with the weak neutral current symmetry in a fairly obvious way, unlike the charged currents, the neutral current has a right handed component. One clear way to resolve this is to add in the electromagnetic current, as its a neutral current with left and right-handed components.

$$j_\mu^{em}(x) = -\bar{e_R}\gamma_\mu e_R - \bar{e_L}\gamma_\mu e_L \tag{2.19}$$

so the the electromagnetic current j_μ can be written using the coupling e

$$j_\mu = e j_\mu^{em} = e\bar{\psi}\gamma_\mu Q\psi \tag{2.20}$$

with Q the charge operator and generator of the $U(1)$ symmetry group of EM. In order to "save" the symmetry of the weak neutral current, we can define an electromagnetic current j_μ^Y, the weak hypercharge current, that is unchanged by $SU(2)_L$ transformations. We define a weak hypercharge Y and its current j_μ^Y

$$Q = T^3 + \frac{Y}{2} j_\mu^Y = \bar{\psi}\gamma_\mu Y\psi \tag{2.21}$$

The combined current

$$j_\mu^{em} = J_\mu^3 + \frac{1}{2} j_\mu^Y \tag{2.22}$$

now generates the symmetry group $U(1)_\gamma$ and so the electromagnetic interaction and weak interaction are combined into one $SU(2)_L \times U(1)_\gamma$. While unified into one enlarged group, the two forces still have independent coupling strengths. This brief introduction into electroweak unification is not the complete picture- EM and weak interactions still have to be unified. This is simple in the Standard model framework- electroweak currents just have to be coupled to vector bosons. In the electroweak $SU(2)_L \times U(1)_\gamma$ group there is an isotriplet of vector fields W_μ^i coupled with strength g to the weak isospin current J_μ^i while a single vector field B_μ is coupled to the weak hypercharge current j_μ^Y with strength $g'/2$. The electroweak interaction can be defined

$$-ig(J^i)^\mu W^i_\mu - i\frac{g'}{2}(j^Y)^\mu B_\mu \tag{2.23}$$

This summary of the unified electroweak force will be the starting point for a derivation of the Higgs boson and an explanation for mass of the weak force's vector bosons (and all fermion masses). The electroweak theory is unique in its calculability, even at higher order scales. Because of this, many deviations from theory could be observed at current energy scales- the theorectical uncertainties are low. The measurement central to my thesis probes for such discrepancies to electroweak theory. The mechanisms for this will be explained in the last section in this section.

Spontaneous Symmetry Breaking

Unlike QED and QCD, the weak force is mediated by massive gauge bosons. Because of this, we can't apply the same gauge invariance prescription that we did in the last sections. If a mass term is added to the Lagrangian we break the gauge invariance we aimed to find. If we instead ignore the gauge invariance and add a mass term to the Lagrangian, all predictive power of the theory is lost due to unrenormalizable divergences. With "spontaneous symmetry breaking" we can gain massive gauge bosons while maintaining the integrity of the theory. In this section I first describe the "spontaneous symmetry breaking" mechanism is terms of an Abelian theory composed of complex scalar fields to illustrate the overall strategy. This mechanism is then applied to the non-Abelian electroweak theory to gain massive weak gauge bosons $W^{+/-}$ and Z, with the Higgs field appearing as a 'spontaneous' result.

The Lagrangian for a $U(1)$ gauge symmetry

$$\phi \to e^{i\alpha(x)}\phi \tag{2.24}$$

As in the QED case, we introduce a gauge field A_μ and covariant derivative $D_\mu = \partial_\mu - ieA_\mu$ to obtain the gauge invariant Lagrangian

$$\mathcal{L} = (\partial^\mu + ieA^\mu)\phi^*(\partial_m u - ieA_\mu)\phi - \mu^2\phi^*\phi - \lambda(\phi^*\phi)^2 - \frac{1}{4}F_{\mu\nu}F^{\mu\nu}. \tag{2.25}$$

In this example if $\mu^2 > 0$ we gain back the QED Lagrangian for a charged scalar particle of mass μ - with an additional self-interaction term. However, if we take $\mu^2 < 0$ the potential $V(\phi^*\phi) = \mu^2\phi^*\phi - \lambda(\phi^*\phi)^2$ now has a non-zero vacuum expectation value (v.e.v.) and there's a set of equivalent minima shown in Figure 2.2. Choosing one of these minima spontaneously breaks the potential's rotational symmetry. Next, we can perturbatively expand the field about a minima through

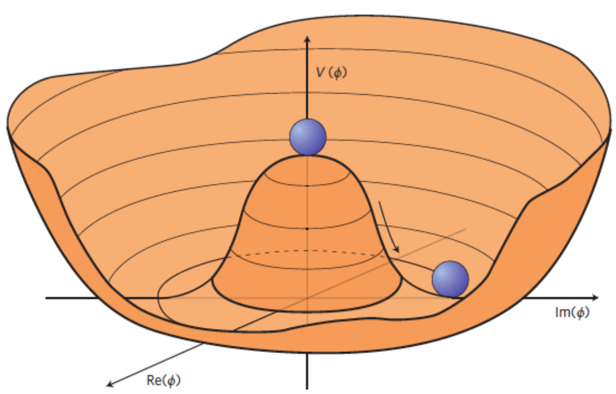

Figure 2.2: Higgs potential when $\mu^2 < 0$, choosing a minima spontaneously breaks the $U(1)$ rotational symmetry (18)

.

$$\phi(x) = \sqrt{\frac{1}{2}[\nu + \eta(x) + i\xi(x)]} \tag{2.26}$$

Substituting this perturbation gives the new Lagrangian

$$\mathcal{L}' = \frac{1}{2}(\partial_\mu\xi)^2+\frac{1}{2}(\partial_\mu\eta)^2-\nu^2\lambda\eta^2+\frac{1}{2}e^2\nu_\mu^A A^\mu-e\nu A_\mu\partial^\mu\xi-\frac{1}{4}F_{mu\nu}F^{\mu\nu}+\text{interaction terms.} \quad (2.27)$$

Three particles seem to emerge here: massless Goldstone boson ξ, massive vector A_μ with $m_A = e\nu$ and a massive scalar η with $m_\eta = sqrt2\lambda\nu^2$. However, the number of particles does not correspond to the polarization degrees of freedom expected, a longitudonal polarization was added, creating an unphysical field. To eliminate the unphysical field we can substitute new set of fields

$$\phi \to \sqrt{\frac{1}{2}(\nu + h(x))e^{i\theta(x)/\nu}} \quad (2.28)$$

and

$$A_\mu \to A_\mu + \frac{1}{e\nu}\partial_\mu\theta. \quad (2.29)$$

Introducing these substitutions, the Goldstone boson field disappears

$$\mathcal{L} = \frac{1}{2}(\partial_\mu h)^2 - \lambda\nu^2h^2 + \frac{1}{2}e^2\nu^2A_\mu^2 - \lambda\nu h^3 - \frac{1}{4}\lambda h^4 + \frac{1}{2}e^2A_\mu^2h^2 + \nu e^2A_\mu^2h - \frac{1}{4}F_{\mu\nu}F^{\mu\nu} \quad (2.30)$$

Here the degrees of freedom before our substitutions remains the same and a massive boson A_μ is preserved along with a massive scalar h. The "Higgs mechanism" applied to a scalar field succeeded in creating a massive boson and determined the existence of a massive scalar boson. This same mechanism can be applied in the more complicated Standard Model electroweak field. Through electroweak symmetry breaking we not only gain massive gauge bosons and a massive scalar boson, (the Higgs!), but a way to calculate testable Standard Model predictions for many quantities. We start with the $SU(2)\times U(1)$ gauge symmetry of electroweak interactions derived in the previous section. In order to gain masses for three gauge bosons and keep the photon massles we need at least 3 degrees of freedom added and a simple choice is the $SU(2)$ doublet of scalar fields ϕ, with four fields in an isospin doublet of weak hypercharge $Y = 1$

$$\mathcal{L} = (D^{\mu}\phi)^{\dagger}(D_{m}u\phi) - \mu^{2}\phi^{\dagger}\phi - \lambda(\phi^{\dagger}\phi)^{2} \tag{2.31}$$

where ϕ is a $SU(2)$ doublet of complex scalar fields

$$\phi = \sqrt{\frac{1}{2}}\begin{bmatrix}\phi_1 + i\phi_2 \\ \phi_3 + i\phi_4\end{bmatrix} \tag{2.32}$$

Local gauge invariance can be achieved just as shown previously with the covariant derivative

$$D_{\mu} = \partial_{\mu} + ig\frac{\tau_a}{2}W_{\mu}^{a} \tag{2.33}$$

with three gauge fields designated with $W_{\mu}^{a}(x)$ and $a = 1, 2, 3$. An infinitesimal transformation is defined

$$\phi(x) \to \phi'(x) = (1 + i\alpha(x) \cdot \tau/2)\phi(x) \tag{2.34}$$

so that we find a Lagrangian potential

$$V(\phi) = \mu^{2}\phi^{\dagger}\phi + \lambda(\phi^{\dagger}\phi)^{2}. \tag{2.35}$$

Once again if we choose the conditions $\mu^2 < 0$ and $\lambda > 0$ there is rotational symmetry in our choice of vacuum expectation value. In this case choice of vev is limited. For the photon to remain massless, the vacuum must be invariant under $U(1)$ (or electromagnetic) transformations, and not be charged in either direction (charge conservation). Thus the chosen minima to spontaneous break electroweak symmetry is

$$\phi_0 = \sqrt{\frac{1}{2}} \begin{bmatrix} 0 \\ \nu \end{bmatrix} \tag{2.36}$$

Next, as before substituting the vacuum expectation value ϕ_0 for $\phi(x)$ and expanding perturbativelyyields

$$\phi(x) \to \begin{bmatrix} 0 \\ \sqrt{\frac{1}{2}(\nu + H(x))} \end{bmatrix} \tag{2.37}$$

Fully expanding this term in the Lagrangian gives a complex and illuminating result, the Goldstone bosons have been consumed and there is only a Higgs field ($H(x)$) remaining. Next, masses for the vector bosons are found from expanding one key parameter in the Lagrangian

$$|(-ig\frac{\tau}{2} \cdot W_\mu - i\frac{g'}{2}B_\mu)\phi|^2 = \sqrt{\frac{1}{2}} \begin{bmatrix} gW_\mu^3 + g'B_\mu & g(W_\mu^1 - iW_\mu^2) \\ g(W_\mu^1 + iW_\mu^2) & igW_\mu^3 + g'B_\mu \end{bmatrix} = \begin{bmatrix} 0 \\ \nu \end{bmatrix} |^2 \tag{2.38}$$

Expanding further and substituting $W^\pm = (W^1 \pm iW^2)/\sqrt(2)$ gives the result

$$|(-ig\frac{\tau}{2} \cdot W_\mu - i\frac{g'}{2}B_\mu)\phi|^2 = (\frac{1}{2}\nu g)^2 W_\mu^+ W^{-\mu} + \frac{1}{8}(W_\mu^3, B_\mu) \begin{bmatrix} g^2 & -gg' \\ -gg' & g'^2 \end{bmatrix} \begin{bmatrix} W^{\mu 3} \\ B^\mu \end{bmatrix} \tag{2.39}$$

It's immediately clear that there's a mass-term for the $W^\pm$, $M_W = \frac{1}{2}\nu g$. Masses for the photon and Z-boson are also apparent after the expansion of the last equations final term

$$\frac{1}{8}\nu^2(g^2(W_3^\mu)^2 - 2gg'W_\mu^3 B^\mu + g'^2 B_\mu^2) = \frac{1}{8}\nu^2(gW_\mu^3 - g'B_\mu)^2 \tag{2.40}$$

and using the substitutions

$$A_\mu = \frac{g' W_\mu^3 + g B_\mu}{\sqrt{(g^2 + g'^2)}} \text{ with } M_A = 0, Z_\mu = \frac{g W_\mu^3 - g' B_\mu}{\sqrt{(g^2 + g'^2)}} \text{ with } M_Z = \frac{1}{2}\nu\sqrt{(g^2 + g'^2)}. \tag{2.41}$$

Now the Higgs field exists just in the previous example and the theory contains a massive scalar boson and three massive vector gauge fields - for each of the W and Z bosons. The Goldstone bosons have been consumed, their degrees of freedom used to give mass to the vector bosons. Choosing a ground state and so breaking the gauge symmetry doesn't eliminate this symmetry altogether, since the theory is still renormalizable. Fermion masses can also be derived from their interactions with the Higgs boson using this Lagrangian. These derivations can be used to predict masses of bosons and fermions and couplings to the Higgs boson. It's important to note that though the Higgs mechanism gives mass to all fermions and massive gauge bosons, it doesn't determine what the Higgs mass ought to be. This is left as an empirical input to the theory with which to calculate other observables.

The Standard Model has been proven over decades to be an incredibly robust theory and Large Hadron Collider (LHC) is it's key testing ground.

2.2 LHC Physics/Phenomenology

The Large Hadron Collider (LHC) is the foremost Standard Model testing ground and the the proton-proton collisions recorded through the ATLAS detector have created greater understanding of the fundamental constants discussed in the previous section. Fermion and gauge boson masses and couplings, including the mass of the Higgs boson, have been measured incredibly precisely. In the next chapter the mechanics of the LHC and ATLAS detector will be discussed, but first here I will introduce the motivations and observations of LHC physics. This section will begin with the mechanics of proton-proton collisions and their decay products, then introduce the concept of decay cross-sections and finally focus more closely on the Higgs boson and its properties.

The LHC was designed with one central goal- discover the missing Standard Model Higgs boson. The protons in the LHC collide at a center-of-mass energy of 14 TeV, but began at half that in 2010. The electroweak symmetry breaking scale was theoretically known to be between 100-1000 GeV and so probing at 7 TeV provided near certainty of finding either the Higgs or an inconsistency in the Standard Model. The motivation for a proton collider was multifaceted. Foremost, using the tunnels built for the electron-positron detector LEP with protons allows the collider to reach higher energies, as protons don't lose energy to synchroton radiation at the same scale as electrons. However, proton collisions have added complexity from their component quarks. Each parton carries some fraction of the momentum of the proton described by parton distribution functions.

Figure 2.3 shows a proton-proton collision schematic. In this example, from (14), the hard process comes from the up quark in each proton. "Hardness" refers to the fraction of momentum of the protons that is involved in the collision. In contrast, "soft" collisions are those from remaining partons in each proton and usually involve low momentum transfer. These soft collisions are considered the underlying event shown in the figure. Proton scatter of partons is the most common hard process at the LHC by far due to the high density of gluons in the proton and the scale of QCD couplings above electroweak.

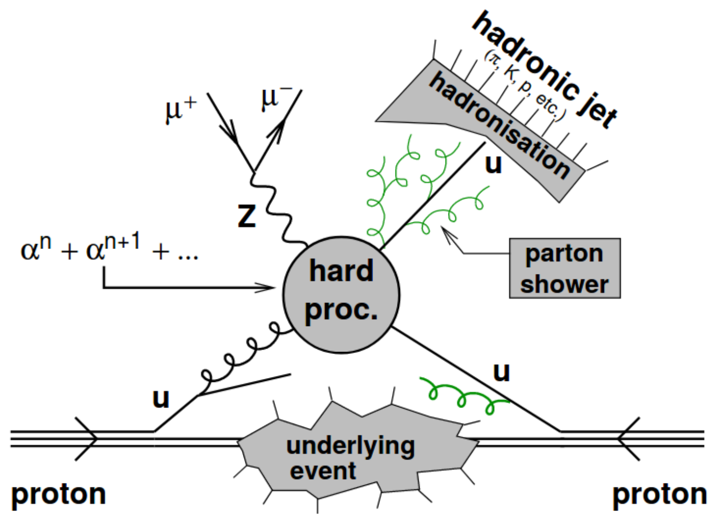

Figure 2.3: Proton-proton collision example showing quark-gluon scattering and final state jet and Z-boson (14)

.

Quarks and gluons emitted from the high energy hard scatter do not appear in the detector directly. QCD, in one of its key differences to QED, becomes stronger with larger distances. As it reaches high enough energy low energy gluons are radiated until partons are able to bind into color-neutral hadrons. These hadrons are seen collimated in groups in the detector as "jets". The energy and momentum of jets are used as reflections of the intial scattered partons. Various "jet algorithms" are used to determine the initial parton properties as reproducibility and precisely as possible. The jet algorithm used in this analysis will be described in detail in Chapter 3. However, it's important to note that the algorithm used by all LHC experiments, anti-k_t- is collinear and infrared safe, or no addected by small angle and soft scatterings that occur in a parton shower. Without these qualities, perturbation theory applied to the parton shower would find infinities at higher orders.

The cross-section (denoted σ) measures the probability that a certain process will occur in the collision of two particles, in our case protons. In high energy physics cross-sections are measured in inverse femtobarns. A barn is the cross-sectional area of a uranium nucleus and was named to describe the large target area needed to have direct strikes on a nucleus. Hence the expression "couldn't hit the broad side of a barn". Inverse femtobarns are used to measure the number of particle collision events per femtobarn area of a target and measures time-integrated luminosity.

Hard scattering cross-sections in hadron-hadron collisions can be calculated using the QCD factorization theorem, and to leading-order these calculations are relatively simple. In the factorization theorem, developed by Drell and Yan, deep inelastic scattering parton model processes could apply to hadron-hadron collisions. The Drell-Yan process is the production of a massive lepton pair by quark-antiquark annihilation. According to the factorization theorem, a hadronic cross-section $\sigma(AB \rightarrow \mu^+\mu^- + X)$ could be calculated by weighting the Drell-Yan sub-process cross-section $\hat{\sigma}$ for $\bar{q}q \rightarrow \mu^+\mu^-$ with parton distribution functions $f_{q/A}(x)$ which come from deep inelastic scattering (15):

$$\sigma_{AB} = \int dx_a dx_b f_{a/A}(x_a) f_{b/B}(x_b) \sigma_{\widehat{ab \rightarrow X}} \tag{2.42}$$

where X represents the two resulting leptons and ab the two annihilated quarks. This parton model provides good agreement with measured cross sections and so allows understanding of particlar hard scattering processes. Predictions for some key Standard Model processes are shown in Figure 2.4. Noting the logarithmic scales it's clear that the Higgs boson of mass 125GeV is orders of magnitude more numerous at the LHC than the Tevatron and that certain high mass particles like the b quark and W/Z bosons are produced at the LHC at high levels (15). In addition, the plot shows cross-sections of particular Higgs decay modes. These will be discussed next.

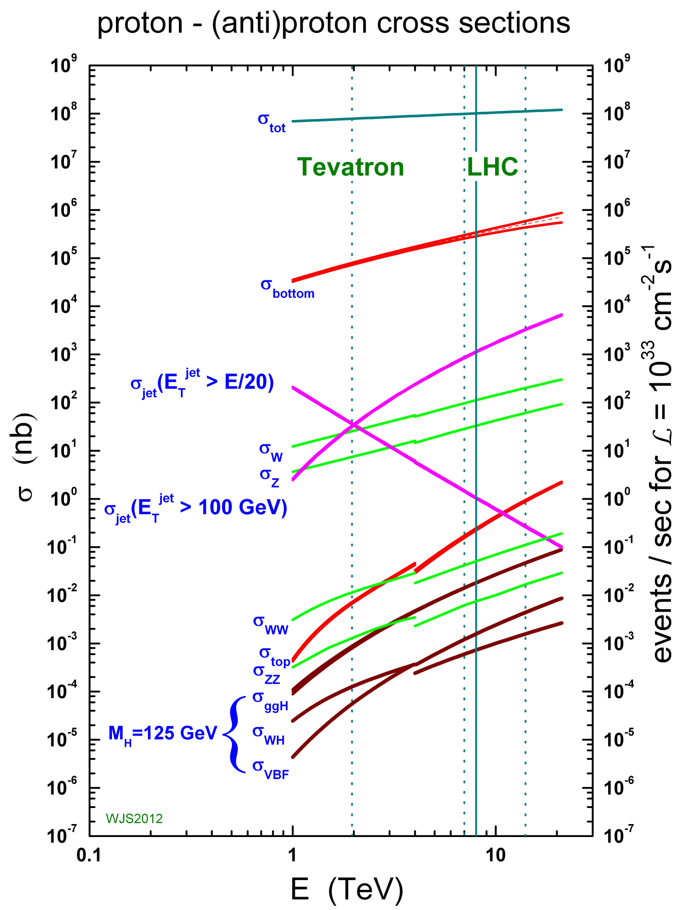

Figure 2.4: Predicted Standard Model cross-sections for the Tevatron and LHC (24).

Higgs production at the LHC occurs via four main processes: gluon-gluon fusion, vector-boson fusion, associated production with W/Z bosons, and associated production with top or bottom quarks. The Feynmann diagrams for these processes are shown in Figure 2.7.

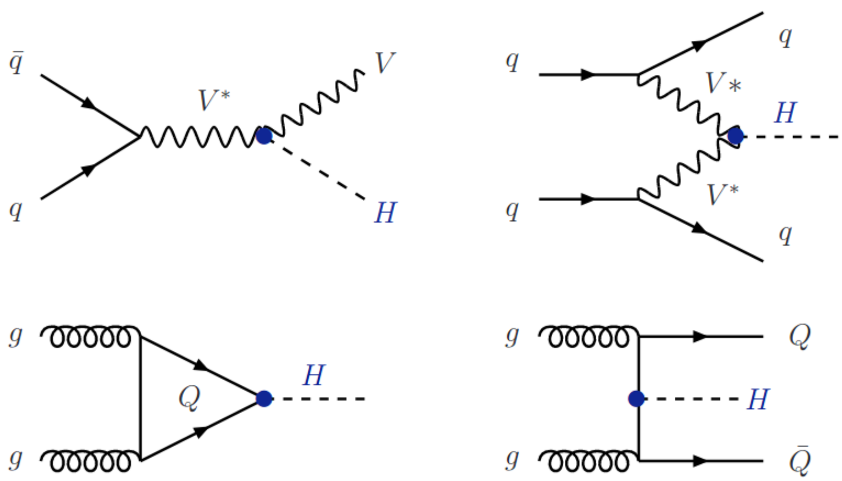

Figure 2.5: Feynmann diagrams for the leading Higgs boson production modes at the LHC (?).

The LHC Cross-section Working Group

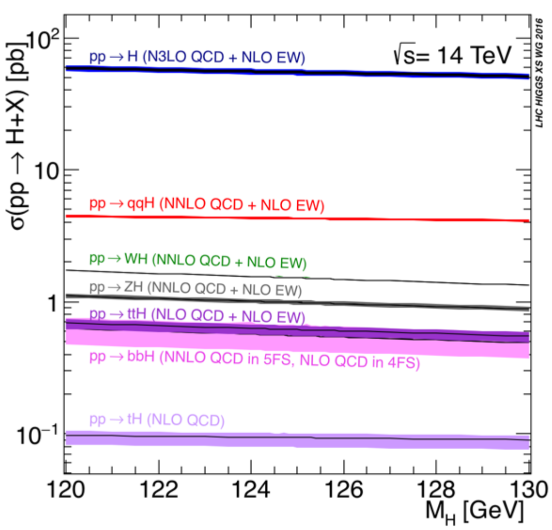

(a) MH

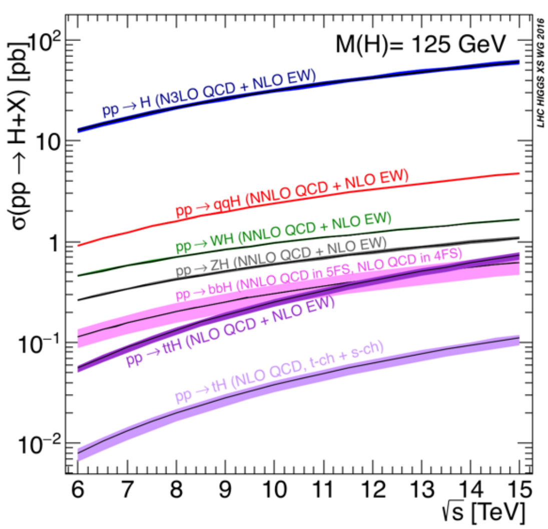

(b) COM

Figure 2.6: Higgs production cross-sections over Higgs mass at center-of-mass energy 14TeV (left) and over center-of-mass energy for a Higgs mass of 125GeV (?)

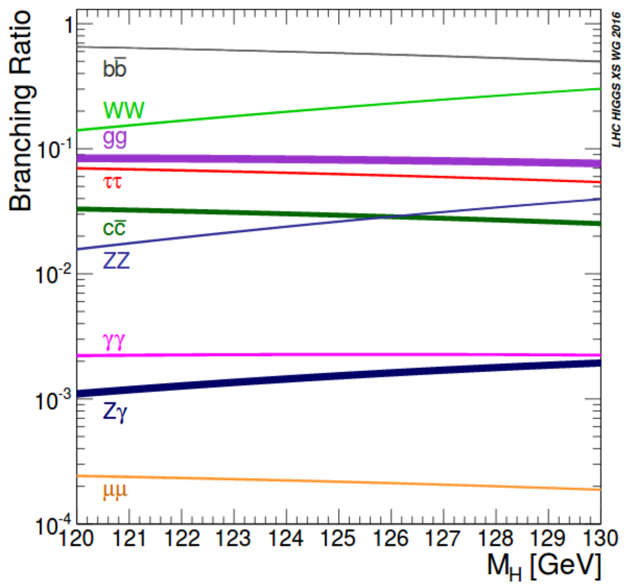

Figure 2.7: Predicted branching ratios for the Higgs boson at the LHC as a function of Higgs mass (**?**).

Decay, search channels

2.3 Brief history of SM tests

first particles weak force QCD bosons Higgs discovery HWW cross section- ATLAS/CMS HWW differential

2.4 Measurement motivation?

Why HWW? Hints from phenomology, why differential? Discuss the future aka the fraction of vbf to SM

Chapter 3

The LHC and the ATLAS detector

3.1 The Large Hadron Collider

The Large Hadron Collider (LHC) is the proton-proton storage ring operating at CERN and for last 13 years has been the world's highest energy particle collider. The LHC first began operation particles in 2008, but following a magnetic quench incident, it had to be repaired and adjusted, so the first data-taking didn't occur until 2009 (22). During the 9 years of LHC operation, protons colliding within each of the experiments were increased to larger center-of-mass energies, approaching the design energy of 14TeV. In addition, luminosity has successively been increased, surpassing design luminosity of $1 \times 10^{34}\text{cm}^{-2}\text{s}^{-1}$ in 2018 to reach $2 \times 10^{34}\text{cm}^{-2}\text{s}^{-1}$(23). The overall data recorded in the ATLAS detector totals more than 10^{16} collisions. The consistent day-to-day operation of the LHC as well as its strides in increasing the energy and number of collisions produced has led to the most precise measurements of Standard Model constants including the coupling of the Higgs boson to bottom quarks (**?**), W and Z bosons (7), (9) as well as photons(8) and tau leptons (6). The LHC has also facilitated searches searches over a wide parameters space, setting confidence level exclusion limits on masses of supersymmetric particles like squarks, gluions and neutralinos (5).

The LHC is set to begin Run 3, in which design center-of-mass energy should be reached, in 2021. Following Run 3, detector upgrades will be made during a long shutdown and then the High-Luminosity LHC (HL-LHC), with unprecedented $10\times$ the luminosity of the LHC, will begin colliding protons in 2027(16). The HL-LHC and its goals will be explained further in **??**, suffice to say that LHC-physics is progressing quickly and promises exciting developments in the near future.

In a brief explanation of the LHC operation, one could begin with the small volume of protons- numbering $\approx 10^{11}$- that is accelerated. Linac 2 is the primary source of protons for CERN accelerators, and has been since the early 1990s (13). This injects protons at 50 MeV into the Proton Synchrotron Booster (PSB) where they are further accelerated to 1.4 GeV. Next they enter the Proton Synchrotron (PS) where the protons are separated into bunches with a spacing of 25 ns and are futher accelerated to 25 GeV before being extracted to the Super Proton Synchrotron (SPS) within which they reach 450 GeV. Finally these bunches of protons enter the LHC and are accelerated to their final energy 6.5 TeV. Linac 2, PSB, PS, and SPS were all operational accelerators prior to being involved in the LHC apparatus, however each had to be majorly upgraded to handle the energy and beam intensity required for LHC collisions (13).

The LHC basic layout mimics that of the Large Electron Positron collider (LEP) that was housed in the same tunnels prior. Figure 3.1 shows the positioning of each experiment on the LHC as well as injection systems and other features. Once proton bunches enter the LHC in two opposing beams they are accelerated with radio frequency (RF) systems. Located at Point 4 in the LHC schematic, the system consists of 16 RF cavities operating at twice the frequency of the SPS injector. RF cavities are metallic chambers containing oscillating electromagnetic fields, in the LHC this oscillation frequency is 400 Mz. The tuning of this frequency ensures that protons of the ideal energy are not accelerated further and simply maintain their maintain their momentum while particles arriving in an RF cavity slightly before or after will be decelerated or accelerated toward the ideal proton energy. This acceleration process can also be used to split beams of protons into discrete bunches, and this is first done with RF cavities in the PS. After proton bunches have circled the LHC approximately 1 million times (15 minutes), peak energy is reached and collisions can commence (4).

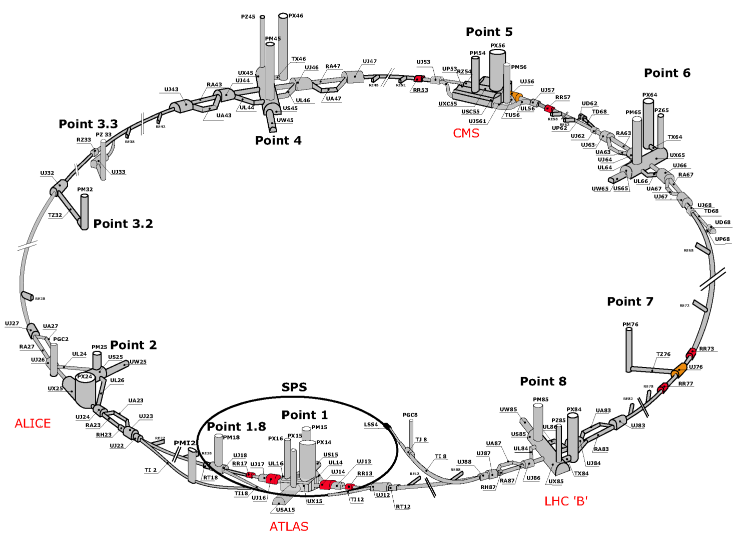

Figure 3.1: LHC layout (19)

Superconducting magnets in the LHC in the main dipoles of the create a magnetic field of ≈ 8T to bend the proton beams into the circular path of the collider. Figure 3.2 shows the flux in a dipole cross-section. The oposing direction beamlines are shown centered and the flux is shown to be high (and directionally opposed) in center of each beam. To maintain these fields, the magnets operate at below 1.9K. Pressurized superfluid helium, chosen for its low visosity and high specific heat, cools the dipole magnets. Once the two LHC rings are filled from the SPS, center-of-mass energy of the beams increase until they reach peak energy after about 28 minutes. Finally, proton bunches separated by 25ns collide simultaneously in each detector.

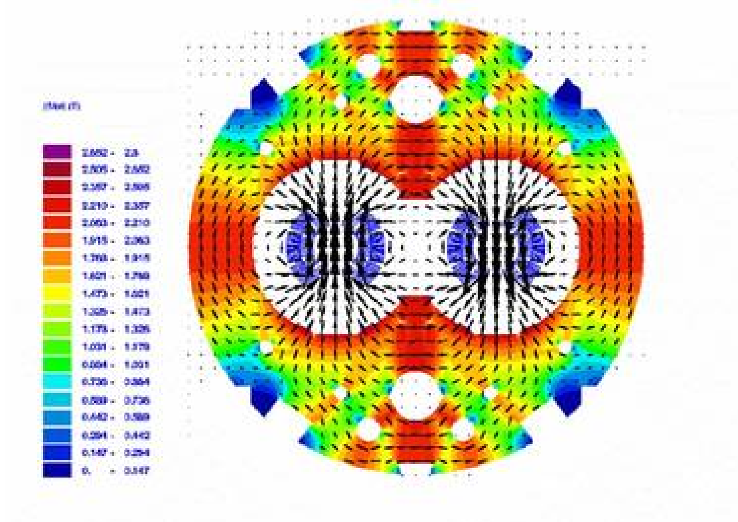

Figure 3.2: Flux within an LHC dipole cross-section (19)

3.2 A Toroidal LHC ApparatuS

The LHC creates proton-proton collisions at a rate and energy level key for pushing the boundaries of particle physics, but identifying and reconstructing the tracks of such energetic particles decay products is no mean feat. A Toroidal LHC ApparatuS (ATLAS) and the Compact Muon Solenoid (CMS) are multi-purpose detectors built to search for and measure a wide range of particle interactions and properties. Both experiments measured a particle consistentwith the Higgs boson in 2012 and their agreement was a key verification of the discovery. The following sections describe each major component of the ATLAS detector with a focus on their use in the measurement of Higgs$\rightarrow WW \rightarrow e\nu\mu\nu$.

ATLAS utilizes a coordinate system with its origin at the center of the detector (the "interaction point") and has a z-axis along the beam pipe. The x-axis points from the interaction point to the center of the LHC ring, and the y-axis points upward. The experiment uses cylindrical coordinates (r, ϕ) where ϕ is the azimuthal angle around the beam pipe. The pseudorapidity and the transverse momentum are defined in terms of the polar angle θ as $\eta = -\ln(\tan(\theta/2))$ and $p_T = p\sin\theta$.

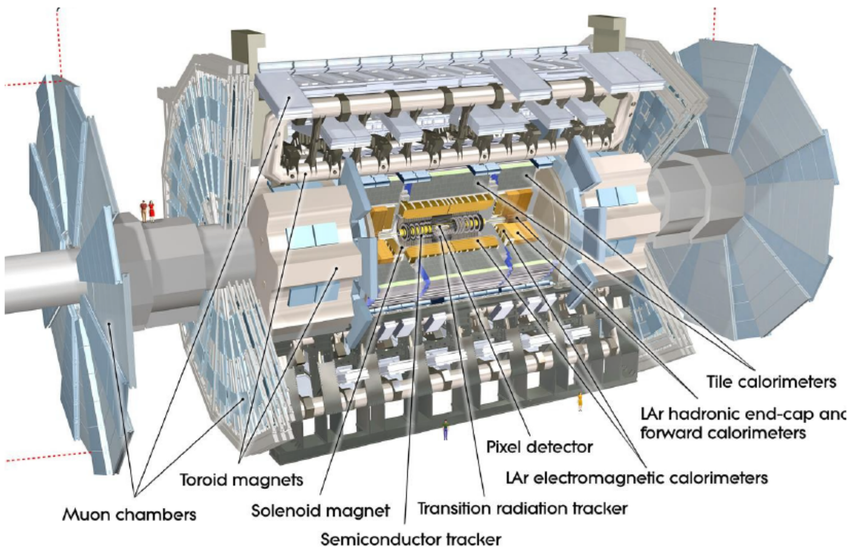

Figure 3.3: Computer-simulated ATLAS detector schematic (det)

The Inner Detector (ID) detects charged particles with an $|\eta| < 2.5$ operating in a 2T solenoidal field. It consists of 3 layers of pixel sensors, 4 layers of silicon strips, and 72 straw layers of transition radiation tracker modules. The ID describes particles closest to the interaction point and detects track parameters with great resolution due to high granularity (det).

The ATLAS detector contains 3 superconducting magnet systems- the barrel toroid, 2 end-cap toriods, and a central solenoid. The central solenoid provides a magnetic field for the inner detector while the toroids create a strong magnetic field for for the muon detector. These magnet systems were built to create the largest possible uniform field (for increased momentum resolution on particle tracks) on a large volume enclosing the detector components. They also need to use as little material as possible so as to not unduly influence particles in the detector. The barrel toroids in the barrel and endcap each have 8 coils and creat e a 4T magnetic field while the central solenoid creates a 2T magnetic field in the inner detector. Combined the magnet systems contain >100km of superconducting wire which are cooled to working temperatures below 5K (det).

The Muon Spectrometer precision chambers provide muon momentum measurements at a high resolution over a wide range of p_T. The MS consists of 3 layers of Monitored Drift Tube chambers covering $|\eta| < 2.7$ and an inner layer of Cathode Strip Chambers with $|\eta| > 2.0$. In addition, it includes trigger chambers that contain 3 layers of Resistive Plate Chambers ($|\eta| < 1.05$) and 3 layers of Thin Gap Chambers ($1.05 < |\eta| < 2.4$). As the outermost subdetector, the MS provides precise muon momentum measurements along the muon trajectory and the muon chambers are located with a precision of under 60 μm. The MS also contains a system of three superconducting toroidal magnets each with eight coils providing a magnetic field with a bending integral of up to 6 Tm (det).

Calorimeters provide detailed information about the energy deposited as particles pass through. Electromagnetic calorimeters detect and halt the motion of electrons and photons while the hadronic calorimeter does the same for hadrons. Muons and neutrinos are able to pass through the calorimeters to the MS. The electromagnetic and hadronic calorimeter, made of liquid Argon and scintillating tiles, respectively, are able to pass information from the location of energy deposits to the muon reconstruction algorithm (det).

3.3 The High-Luminosity LHC and Inner Tracker (ITk)

Though the LHC succeeded in one of its crucial goals of discovering the Higgs boson in 2012, its continuous operation at higher energy and luminosity has led to more rigorous measurements of the Higgs as well as searches for new physics beyond the Standard Model. The LHC has been the leading high energy collider in terms of person power, energy, and scale for over a decade and will continue to be extremely important for understanding theoretical questions in the future. While more data collection is planned in Run-3 starting in 2021 ??, new colliders and detectors take decades to design, develope and build, so the plans for the collider to take it's place is well underway. The High Luminosity LHC will operate at an LHC-level energy (14TeV) and begin data-taking in 2026. The HL-LHC will begin with $5-7\times$ the luminosity of the LHC and will have a design luminosity of $10\times$ the LHC, or $12.6\times10^{-34}\text{cm}^{-2}\text{s}^{-1}$. This huge increase in number of collisions requires massive upgrades to the LHC including new, 11-12T superconducting magnet systems, compact superconducting caivities for beam rotation and phase control, and new technology beam collimation (**?**). This massive undertaking has been underway for many years already and has involved laboratories all over the world.

Just as the LHC had to be re-designed and built to create higher luminosity, so too do all the experiments on the LHC have to be redesigned to be able to interpret so many more collisions per second. The detectors must be built to withstand more radiation, as the increased collision rate also means a high radiation rate especially closest to the beamline. They also have to provide greater granularity to be able to reconstruct tracks with good enough resolution that individual tracks can be discriminated. Finally, they have to be able to deal with increased pile-up. Pile-up is caused by high numbers of collisions occuring at each bunch crossing. When there is a large amount of pile-up it becomes difficult to trace which particle tracks come from the same interaction point. Finally, the increased data in and of itself creates a complex problem for the detectors to solve, as briefly discussed previously, the trigger system must quickly choose which collision events may hold interesting events and store these. When there are more events happening near simultaneously these systems must make these decisions in real-time. New algorithms to speed up this process are necessary when there are an order of magnitude more events to sort through.

Detectors for high energy colliders are not built often- expensive and time-consuming to design and test, they're made to last at least a decade. I was lucky to have the opportunity to work on ATLAS detector research and development during a year I worked at Brookhaven National Laboratory during my Ph.D. and though my thesis isn't directly related to this work, it was formative and extremely interesting, so I'll touch on this work in the next section. Because I worked on the new ATLAS inner detector for the HL-LHC (termed Inner Tracker or ITk) I will just discuss this sub-detector and the particular role I played in its assembly.

3.3.1 Inner Tracker (ITk)

The Inner Tracker is planned to be an all-silicon detector that will completely replace the current Inner Detector. While the current ID has been extremely successful during Runs 1 and 2 (and will certainly continue to be in Run 3), it does not have to capacity to withstand the radiation and pile-up conditions of the HL-LHC. The ITk is designed to operate for 10 years under instantaneous luminosity of $7.5\times10^{-34}\mathrm{cm}^{-2}\mathrm{s}^{-1}$ with 25ns between bunch crossings. This will result in 1,000 fb^{-1} and average pile0up up to $<\mu>= 200$ (17). The current solenoid magnet will remain in the detector with a 2T magnetic field. The ITk will consist of an innermost section with silicon pixels and an outtermost section of silicon strips. The pixel detector will contain four barrel layers and six forward region disks, while the strip detector will contain five barrel layers and seven disks. The rapidity range matches the coverage of the Muon Spectrometer with $|\eta| < 2.7$, this layout is shown in **??**.

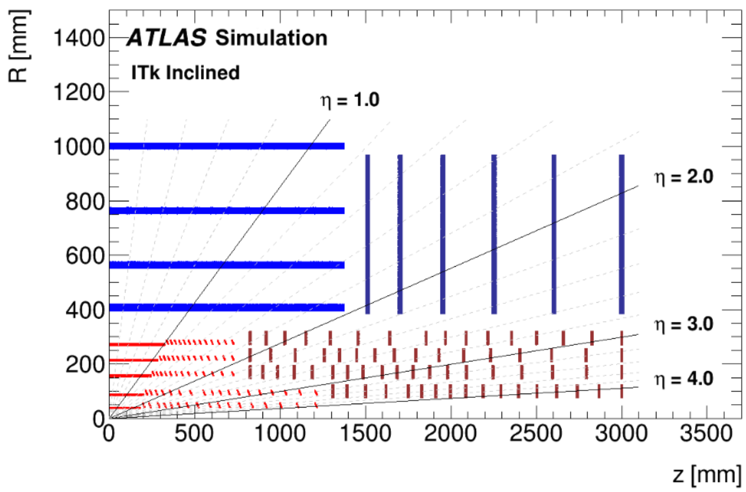

Figure 3.4: ITK layout as defined in Technical Design Report (17)

Building ITk Strip barrel staves

I spent 1.5 years of my Ph.D. at Brookhaven National Laboratory (partially funded through a SCGSR Fellowship) and was able to make key contributions to the ITk Strip barrel stave assembly effort. The goal of stave assembly is to precisely calibrate specified positions for silicon modules on carbon fiber stave cores and then glue them in place within a 25μm tolerance. Brookhaven National Laboratory is responsible for assembly of half off all ITk staves (200) and the accurate assembly is necessary for the ITk to reduce uncertainty on track positions and to ensure a symmetric detector. At Brookhaven, I was tasked with co-creating a stave assembly software system through LabView to automatically calibrate required module positions, apply a layer of adhesive gel, and guide the user to accurately place the module into its specified location. This project was highly collaborative and evolved further after I left the laboratory, but the overall process remains unchanged.

The basic design of the Inner Tracker for both barrel and endcap components is the same - a carbon fiber core (containing titanium cooling pipes) is covered on each side with co-cured kapton service tapes. The carbon fiber core is designed to reduce overall radiation length and the similar design in the barrel and endcap adds to simplicity. Silicon modules are glued to stave cores. Similar radial silicon strip detectors have been used previously in both ATLAS and CMS but never covering so much fiducial area. The modules consist of one silicon sensor and one or two low-mass PCB's (hybrid) which host ASICs. Module design has optimized producibility and low cost while maintaining readout goals. Overall module design is the same in barrel and endcap regions, while strip lengths and geometries vary. Compnents of a short-strip barrel module are shown in 3.5.

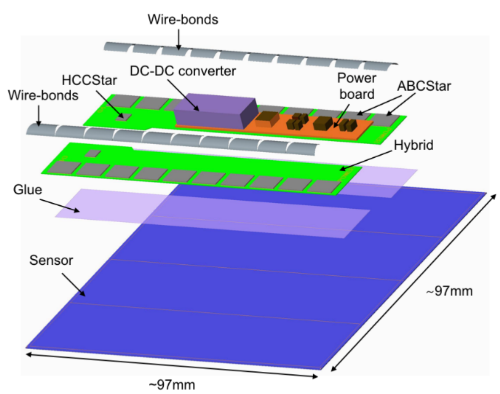

Figure 3.5: Short-strip barrel module components (17)

Each barrel stave core needs to be "loaded" with 14 modules, as shown in the assembled electrical prototype in 3.6. The placement of these modules needs to be accurate to below 25μm so that the detector is symmetrical and ITk models accurately demonstrate particle track positions. After the detector is assembled and commisioned tests will be done with laser alignment to understand the exact positioning of the modules and staves but any module positioning out of specification will have adverse affects on track resolution during operation.

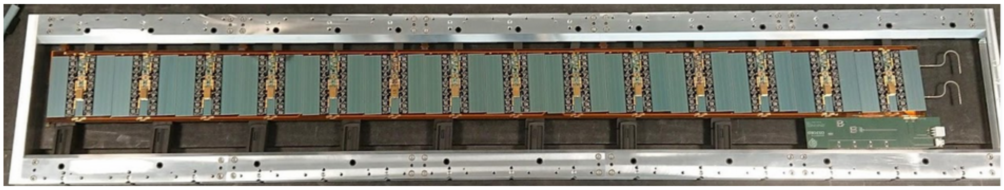

Figure 3.6: Electrical stave prototype at BNL

Brookhaven National Laboratory is one of two sites resposible for assembling barrel staves and their assembly procedures have been tested with the production of numerous prototypes including a thermomechanical double-sided stave and a fully operational electrical stave. The thermomechanical prototype was later used for various thermal tests, including IR imaging (documented in the next section), and the electrical stave is currently undergoing tests for read-out. Stave assembly is composed of three main parts- system calibration, module placement, and survey of results.

Staves at BNL are assembled on a granite table housing an Aerotech XYZ Stage (accurate to the micron level). The stage is equiped with a 10-megapixel camera that gives real-time feedback to a nearby computer and a glue dispenser. The stave assembly software system is implemented by a user who interacts with the LabView GUI and monitors progress. The stave is fixed to optical rails drilled into the table. In order to accurately place modules in their correct positions a series of calibrations need to be completed including camera calibrations to test the optimal working point, focus, and pixel-to-micron conversion. Next, the position of the stave with relation to the XYZ stage needs to be calibrated. Tranforming coordinates of the XYZ stage to that of the stave and so specified coordinates for modules atop their carbon fiber cores requires locating a fixed point on the stave core as well as the angle of the stave relative to the XYZ stage. Pattern matching algorithms find the exact locations of particular features on the stave core and allow calculation of required positions for all modules based on specifications. Once specified module positions are calculated, calibrations are complete and it's time to apply glue and afix modules.

Next, an epoxy (SE4445) is loaded into the glue dispenser on the XYZ-stage which is connected to a vaccuum controlled by the LABView software system. The epoxy is automatically dispensed in lines to cover $\approx 60\%$ of area under the module and then the module is lifted with a custom-made "pick-up" tool which uses a vacuum applied to module corners to hold the module in place and move it to the needed position along the optical rails. Then, using real-time feedback from the software system and its pattern matching algorithm the user is directed on how to finetune the positon of the module using knobs on the "pick-up" tool. Markings etched in the silicon sensor at each corner which are used to position the module accurately. The output of the module alignment GUI is shown in **??**. When the module is within specifications it is lowered into position above the epoxy and held in place for 24 hours until the glue has completely dried.

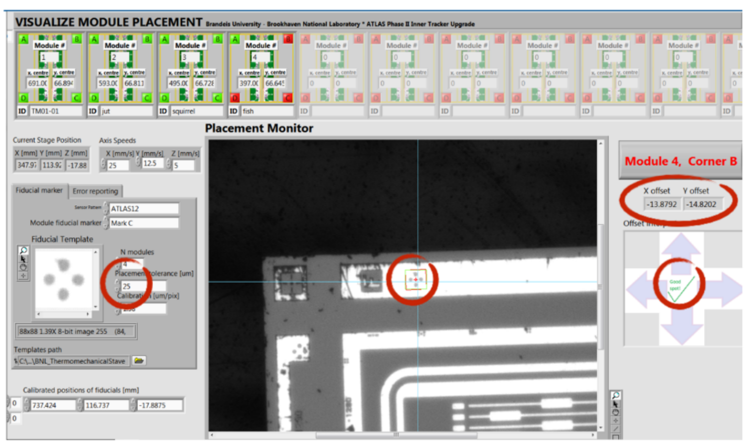

Figure 3.7: GUI interface showing etched marking on module corner located in real-time to guide user on how to adjust module position

Finally, after the glue has set, a final survey of module positions (taken by using pattern matching to find the positions of etched markings on each corner) is taken. These results are saved into an ITk database and checked for any biases. After module placement on the stave is complete, it is moved to another station in the lab for wirebonding so that all data from the modules can be read-out to stave-wide electronics and then moved off detector. The module assembly system has worked quite well at placing modules accurately for all prototypes, achieving specification requirements for almost all modules. Results of the first prototype stave module placement are shown in 3.8. While a few module corners are slightly out of the ideal range, the majority are well within specifications. While building prototypes, some issues and inefficiencies were found and corrected. New hardware, like an improved glue system temperature monitoring were also added during prototype assembly. The methods described continue to be in use now and will be utilized for the production of 200 ITk staves at BNL.

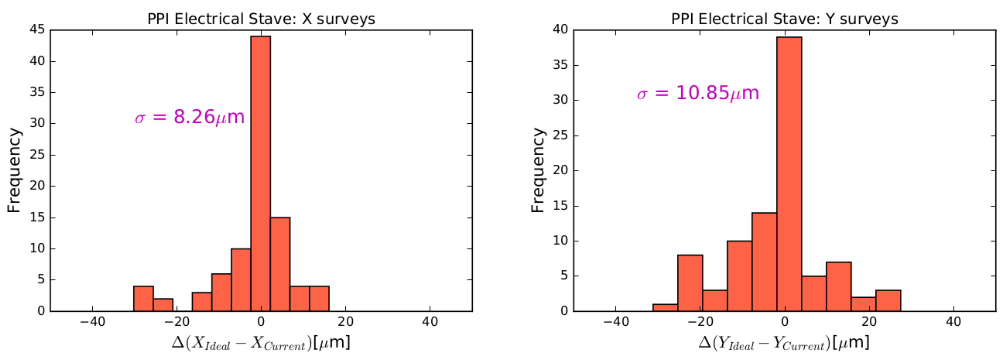

Figure 3.8: Histograms show difference between ideal and final position of each module corner. Left shows difference from specification in X and right in Y.

IR Testing ITk Strip barrel staves

The first full US stave prototype is the thermo-mechanical stave, built in the summer of 2017. Building this stave was the first test of the stave assembly procedure and methods and the results showed success. This stave was also assembled to test the thermal and mechanical properties of a fully loaded barrel stave. Multiple tests were done including thermal studies (using thermistors and IR imaging), thermal cycling and thermal shock tests, mechanical studies, and bending tests. I will give a short summary on IR imaging tests, as these were another focus of my time at BNL. First, the thermo-mechanical stave consists of 13 modules mounted on each side. The modules used are thermo-mechanical, which means that instead of the usual readout chips their hybrids have copper traces to mimic the power dissipation and location of the chips. The powerboard can vary the TM hybrid power dissipation of each module individually. In addition, these modules each have three thermistors- one of the DC-DC converter, and one on each of two hybrids. The stave is powered by a custom End-of-Substructure (EoS) card which is attached to a RaspberryPi and Arduino and can power on or off each module.

Thermal testing of barrel staves had a few main goals: first, to compare with Finite Element Analysis simulations and so test that all temperature trends are as we expect, to make sure that individual modules- and their slightly modified assembly methods- don't exhibit abnormal thermal behavior, and finally to check that loaded staves can cope with potential issues they might face during operation. I will highlight a few key results which demonstrate that each of these goals have been accomplished.

Thermal measurements were taken both through the mounted thermistors on each module and through IR imaging. IR imaging provides information about the entirety of the loaded stave, rather than at just a few module positions so provides a more complete picture. The loaded stave was spray-painted black with a high emissivity, low conductivity black paint since silicon is transparent to the IR camera spectrum (8-14μm). In order to image the entire stave core, the IR camera was attached to rails above and pulled at a constant speed with an external motor as it recorded video. The frames were then stitched together into one image. A section of the painted stave is shown in 3.9.

FEA simulations for the thermal performance of a stave were completed by Prof. Graham Beck at QMUL. These calculations quickly became intractable if convection was included, so

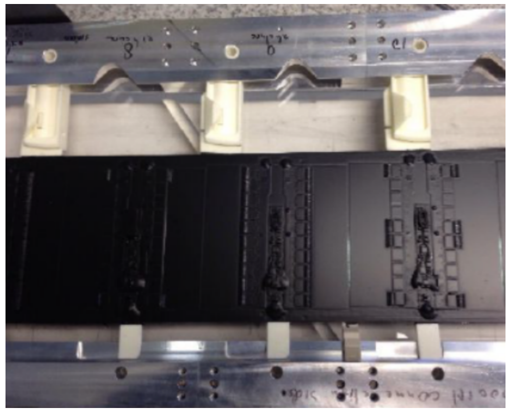

Figure 3.9: Portion of the thermo-mechanical stave after spray-painted for increased emissivity

conditions of the stave and coolant were adjusted such that convective constributions were minimal, or the total electrical power and power absorbed into the coolant were identical. At BNL we adjusted the coolant temperature until we saw this convective power minimization, then recorded module temperatures under these conditions. These results were compared to the FEA simulations by averaging hybrid temperatures recorded through IR imaging and recording NTC thermistor readings. These comparisons are shown in 3.10. The measurements show very good agreement with FEA calculations, within 5% of the expected values.

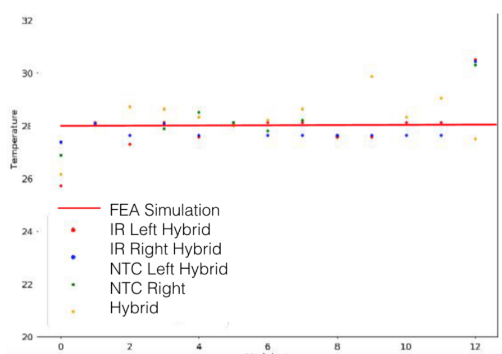

Figure 3.10: IR measurements, NTC thermistor measurements, and FEA simulations for the TM stave are compared. Agreement with expected within 5%

During module assembly some slight variations were tested including varying glue thickness below modules and glue curing time, and FEAST versions. Module with these variations were noted and compared to those without at varying coolant temperatures and output power settings. Overall, no significant differences in module temperature change was observed for any of these assembly modifications. Fully loaded stave thermal properties are thus robust to assembly modifications like these. Figure 3.11 shows a full IR image of the fully loaded stave. It's clear that there are no obvious module-to-module variations in silicon, hybrid, or FEAST temperature. The module sensors increase in temperature as they get closer to the EoS, which is expected since it dissipates power to the stave.

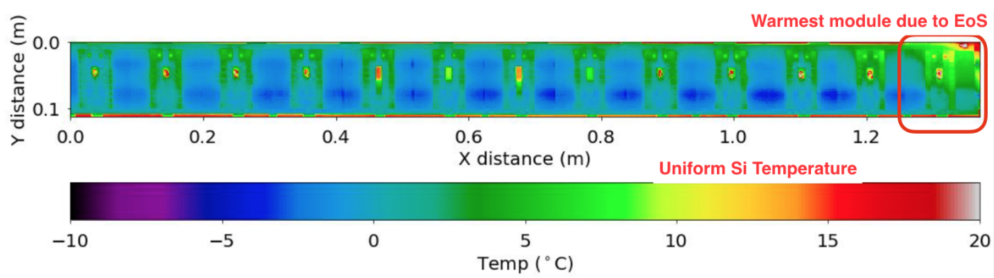

Figure 3.11: IR image of fully loaded thermo-mechanical stave

The thermo-mechanical stave was pushed to limits beyond what we would expect loaded staves to encounter during operation and never exhibited unexpected behavior. Thermal cycles, thermal shocks and bend tests showed the loaded stave robust to intense temperature variation and that the carbon fiber core is as stiff as it was prior to loading. Another test was how neighboring modules would perform if one module malfunctioned and went offline. Figure 3.12 shows temperature of each module when one of them (fourth to the left) turns off. The rest of the modules continue to operate normally and temperature changes from the unpowered module don't propagate very far. The second image in the figure shows the reverse of the stave when a module is powered off (fourth from the right). The temperature effects are greater directly below than adjacent to- which is expected.

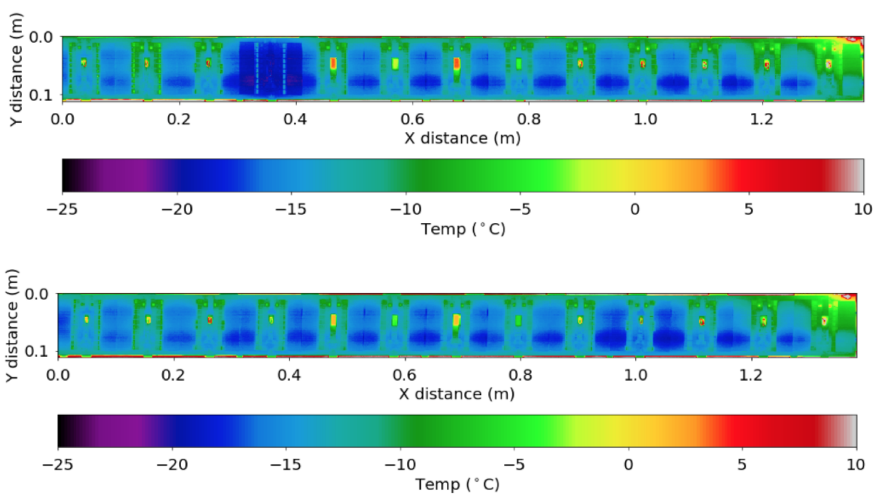

Figure 3.12: IR image of fully loaded thermo-mechanical stave

Chapter 4

Tracking and Isolation in ATLAS

4.1 Tracking and isolation in ATLAS

4.1.1 Jets

4.1.2 MET

4.1.3 Electrons

4.1.4 Muons

Muons are abundant in the ATLAS detector and help lead to some of the most interesting physics results and analyses produced by the ATLAS experiment, for example, $H \rightarrow 4\ell$ or $Z' \rightarrow \mu^+\mu^-$ searches (10). The Muon Combined Performance group is tasked with producing the most accurate muon data for physics analyses. This includes muon reconstruction, identification, isolation, and analysis of efficiency, as well as muon momentum scale and resolution. The group's goal is to create a number of "working points" tailored to different types of physics analyses that will isolate, identify, and reconstruct muons in the region of interest to the analyses. The working points are continuously updated and improved before being tested and implemented on different analyses. My work with the MCP group has focused on applying corrections necessary for muon momentum scale at the per mille level and resolution at the percent level in simulation/data. These are derived by a template fit of simulations smeared and corrected by variables in data. Finally, these corrections are validated by comparisons to simulations over a variety of variables.

Muon reconstruction is performed independently in the ID and MS and the information from these separate sub-detectors is combined to form full tracks. This section will focus on: 1) reconstruction in the ID, which is the same for any charged particle; 2) reconstruction in the MS, which is particular to muons; and 3) the combined reconstruction, which uses information from both the ID and MS.

Muon reconstruction in the ID

In the ID, a pattern recognition algorithm reconstructs particle tracks with an inside-out sequence (21). A track from a particle traversing the barrel typically has 3 pixel clusters, 8 SCT clusters and more than 30 TRT straw hits. The sequence begins by finding three-dimensional space points from the silicon hits. Each set of three space points which originate in the interaction point are used to trace hits up to the outer edge of the silicon detector. The final track parameters are fit through a collection of hits that extend to the TRT (3).

Muon reconstruction in the MS

Muon reconstruction in the MS is not an inside-out procedure like that in the ID. Reconstruction begins with a search for hit patterns in each MS subdetector, which are called segments. The middle of the MS typically exhibits the largest number of trigger hits, therefore tracks are built by working out from the center of the MS and connecting segments layer-by-layer. Criteria such as hit multiplicity and fit quality determine track acceptance. At least two segments are needed to build a track. Hits associated with each track candidate are fitted using a global χ^2 fit. A track candidate is accepted if it passes the selection criteria (**?**).

Combined Reconstruction

The combined ID-MS reconstruction uses different algorithms to find different *muon types*. There are four main types outlined below, but preference-in terms of overlap between types-is given to Combined (CB), then Segment-tagged (ST), and finally Calorimeter Tagged (CT) muons. These algorithms have been continuously been improved to yield better precision, speed, and robustness against misidentification (12).

- **Combined muon (CB)**: This type combines tracks from the ID and MS detectors using a global refit on all hits (some may be removed or added to improve quality). Most muons are reconstructed using an outside-in method.

- **Segment-tagged muon (ST)**: ST muons are assigned an ID track that is associated with at least one local MDT or CSC track after extrapolation. These are used when muons cross only one layer of the MS because of low p_T or regions out of most MS layer boundaries.

- **Calorimeter-tagged muon (CT)**: These muons are identified by an ID track that can be matched to a minimum ionizing particle energy deposit in the calorimeter. These muons have the lowest purity but are optimized for $|\eta| < 0.1$ and $1.5 < p_T < 100$ GeV where the MS is only partially instrumented.

- **Extrapolated muon (ME)**: These muons are reconstructed in the MS with the addition of silicon points and with a loose requirement that the muon track originated at the IP. In general, this muon is required to traverse $2-3$ layers of MS chambers. These are mainly used to extend acceptance for $2.5 < |\eta| < 2.7$, which is not covered in the ID.

Muon Identification

In order to identify muons from other particles (like backgrounds from pion and kaon decays) strict quality requirements must be set to select prompt muons with high efficiency. Ideal "signal" muons are those that come from W decays (as opposed to light-hadron decays) and originate from the interaction point. We use a few variables to identify muons:

- *q/p significance*: The absolute value of the difference between the ratio of the charge and momentum of muons in the ID and MS divided by the sum in quadrature of their corresponding uncertainties.
- ρ': The absolute value of the difference between the p_T measurements in the ID and MS divided by the p_T of the combined track.
- χ^2: The normalized fit parameter of the combined track.

Specific requirements on the number of hits in the ID and MS assure that inefficiencies are expected and momentum measurements are robust. There are four muon identification selections that each addresses specific needs of physics analyses (12).

- ***Loose* Muons**: The *Loose* criteria maximizes the reconstruction efficiency, losing very few potential muons, while providing satisfactory tracks. All muon types are used in this criteria, and it is the optimal selection for Higgs boson candidates in the four-lepton final state (10).

- ***Medium* Muons**: *Medium* is the default selection for muons in ATLAS because it minimizes systematic uncertainties associated with reconstruction and calibration. Only CB and ME tracks are used with requirements for over 3 hits in at least two MDT layers in most regions. All *Medium* muons are included in the *Loose* criteria.

- ***Tight* Muons**: *Tight* selects muons with the highest purity, but sacrifices efficiency. All *Tight* muons are included in the *Medium* selection, but only CB muons with at least two hits in the MS are considered, and the χ^2 value must be less than 8.

- ***High-p_T* Muons**: *High-p_T* muons have good momentum resolution for tracks with $p_T > 100$ GeV. This is beneficial to searches for high-mass Z' and W' resonances. CB muons in the *Medium* selection with at least 3 hits in 3 MS stations are included.

Muon Reconstruction Efficiency

We measure the muon reconstruction efficiency in two different ways in the regions $|\eta| < 2.5$ and $2.5 < |\eta| < 2.7$. First, in the barrel region, we use the **Tag-and-Probe** method. In this method we select an almost-pure sample of J/ψ and Z decays. We require the leading muon to be a *Medium* muon labeled the **tag**. This muon fires the trigger. The subleading muon, the **probe**, must be reconstructed independently. There are three types of probes:

- **ID track**: Allows measurement of MS efficiency and of tracks not accessible to CT muons.

- **CT tracks**: Allows measurement of MS efficiency and has powerful rejection of background (especially at low p_T). This is the most commonly used probe.

- **MS tracks**: Allows measurement of ID and CT efficiency.

To find the overall efficiency of *Medium, Tight,* or *High-p_T* muons, we multiply the efficiencies associated with each type of probe. The efficiency ϵ(X|CT) (X = *Medium / Tight / High-p_T*) of reconstructing these muons assuming a reconstructed ID track is measured using a CT muon as probe. This result is corrected by the efficiency ϵ(ID|MS) of the ID track reconstruction measured using MS probes.

$$\epsilon(\mathrm{X|ID}) \cdot \epsilon(\mathrm{ID}) = \epsilon(\mathrm{X|CT}) \cdot \epsilon(\mathrm{ID|MS}) \qquad (\mathrm{X} = Medium/Tight/High\text{-}p_T)$$

The ID track reconstruction efficiency must be independent from the muon spectrometer track reconstruction ($\epsilon(\mathrm{ID}) = \epsilon(\mathrm{ID|MS})$). In addition, the use of a CT muon as a probe instead of an ID track must not affect the probability for *Medium, Tight,* or *High-p_T* reconstruction ($\epsilon(\mathrm{X|ID}) = \epsilon(\mathrm{X|CT})$). These assumptions are largely true with simulations showing some small deviations. These deviations are taken into account when calculating systematic errors. The reconstruction efficiency of *Loose* muons is measured separately for CT muons within $|\eta| < 0.1$ and all other *Loose* types. The CT muon efficiency is measured using MS probe tracks, and the efficiency of other muons is evaluated similarly to the *Medium, Tight,* and *High-p_T* muons using CT probe muons (12). For $|\eta| > 2.5$, the efficiency is calculated using the ME muons in the **Loose** and **Medium** selections. The number of muons observed in this region is normalized to the number of muons observed in the region $2.2 < |\eta| < 2.5$. A more detailed discussion of the efficiency measurement in this region can be found in Ref. (old). **Scale factors** are defined as the ratios between the efficiency of data and the efficiency of Monte Carlo simulations. They are used to describe the deviation between simulated and real detector behavior and are used in physics analyses to correct simulations.

Figure 4.1 displays reconstruction efficiency for *Medium* muons over a range of p_T and η. J/ψ decays probe low p_T muons while Z decays probe muons of a higher p_T allowing a large

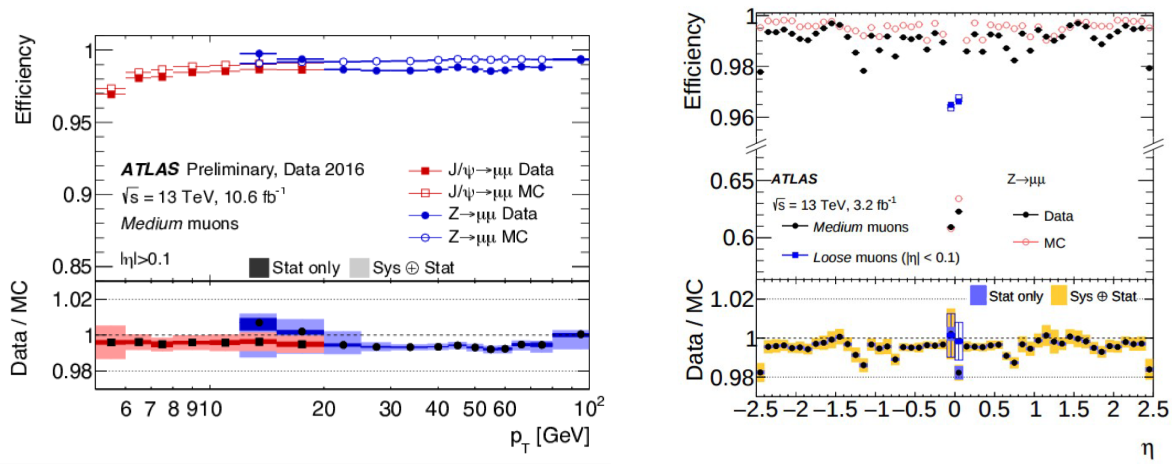

Figure 4.1: On the left, reconstruction efficiency for *Medium* muons from $Z \to \mu\mu$ and $J/\psi \to \mu\mu$ events is displayed as a function of the p_T of the muon in the region $0.1 < |\eta| < 2.5$. On the right, muon reconstruction efficiency is shown as a function of η in $Z \to \mu\mu$ events for muons with $pT > 10$ GeV for *Medium* and *Loose* muons (squares) in the region $|\eta| < 0.1$, where the *Loose* and *Medium* selections differ significantly. In both plots the error bars on the efficiencies indicate the statistical uncertainty and the bottom panels show the ratio of the measured to predicted efficiencies, with both statistical and systematic uncertainties (12).

range to be defined. Muon reconstruction works well over a large range of both p_T and η as evidenced by an efficiency above 95% throughout ranges shown in p_T and η. In addition, MC simulations match data quite well - within $1-2\%$. The only significant loss of efficiency is seen with *Medium* muons at extremely low η due to criteria excluding ID muons. We can make up this lost efficiency by substituting *Loose* muons for excluded ID muons. Overall, the default *Medium* muon selection demonstrates a high reconstruction efficiency.

Muon Isolation

Isolating muons from heavy particles is one of the keys to understanding the background in many physics analyses. When heavy particles like W, Z, and Higgs bosons decay they often produce muons in isolation. Semileptonic decays, on the other hand, typically produce muons embedded in jets.

The MCP group uses two muon isolation variables: a track-based variable ($p_T^{varcone30}$) and a calorimeter-based variable ($E_T^{topocone20}$). $p_T^{varcone30}$ is defined as the scalar sum of the transverse momenta of tracks with $p_T > 1$ GeV in a cone around the muon of transverse momentum p_T excluding the muon track itself. The cone size is p_T-dependent to improve the performance for muons produced in decays with a large transverse momentum. $E_T^{topocone20}$ is defined as the sum of the transverse energy of topological clusters in a cone around the muon after subtracting the contribution from the energy deposit of the muon itself and correcting for pile-up effects (11).

Table **??** defines seven isolation selection criteria - called "isolation working points" - that optimize different physics analyses. The*LooseTrackOnly* and *FixedCutTightTrackOnly* working points are defined by cuts on the relative track-based isolation variable. All other working points are defined by cuts applied separately on both relative isolation variables. All cuts are tuned as a function of the η and p_T of the muon to obtain a uniform performance. The target efficiencies of the different working points are described in Table 4.1. The efficiencies for the seven isolation working points are measured in data and simulation using the **Tag-and-Probe** method described in Section 4.1.4 on $Z \to \mu\mu$ decays. Figure 4.2 shows the isolation efficiency measured for *Medium* muons in data and simulation as a function of the muon p_T for two different working points. In both the *Loose* and *LooseTrackOnly* working points, efficiency is above 98% and matches simulation well within errors.

Muon Momentum Corrections

The muon momentum scale and resolution are studied using Z and J/ψ decays. In order to obtain agreement between simulation and data in muon momentum scale to the per mille level and in resolution to the percent level, we need to apply a set of corrections to the

Isolation WP	Discriminating variable(s)	Definition
LooseTrackOnly	$p_{\mathrm{T}}^{\mathrm{varcone30}}/p_{\mathrm{T}}^{\mu}$	99% efficiency constant in η and p_{T}
Loose	$p_{\mathrm{T}}^{\mathrm{varcone30}}/p_{\mathrm{T}}^{\mu}$, $E_{\mathrm{T}}^{\mathrm{topocone20}}/p_{\mathrm{T}}^{\mu}$	99% efficiency constant in η and p_{T}
Tight	$p_{\mathrm{T}}^{\mathrm{varcone30}}/p_{\mathrm{T}}^{\mu}$, $E_{\mathrm{T}}^{\mathrm{topocone20}}/p_{\mathrm{T}}^{\mu}$	96% efficiency constant in η and p_{T}
Gradient	$p_{\mathrm{T}}^{\mathrm{varcone30}}/p_{\mathrm{T}}^{\mu}$, $E_{\mathrm{T}}^{\mathrm{topocone20}}/p_{\mathrm{T}}^{\mu}$	$\geq$ 90(99)% efficiency at 25 (60) GeV
GradientLoose	$p_{\mathrm{T}}^{\mathrm{varcone30}}/p_{\mathrm{T}}^{\mu}$, $E_{\mathrm{T}}^{\mathrm{topocone20}}/p_{\mathrm{T}}^{\mu}$	$\geq$ 95(99)% efficiency at 25 (60) GeV
FixedCutTightTrackOnly	$p_{\mathrm{T}}^{\mathrm{varcone30}}/p_{\mathrm{T}}^{\mu}$	$p_{\mathrm{T}}^{\mathrm{varcone30}}/p_{\mathrm{T}}^{\mu} < 0.06$
FixedCutLoose	$p_{\mathrm{T}}^{\mathrm{varcone30}}/p_{\mathrm{T}}^{\mu}$, $E_{\mathrm{T}}^{\mathrm{topocone20}}/p_{\mathrm{T}}^{\mu}$	$p_{\mathrm{T}}^{\mathrm{varcone30}}/p_{\mathrm{T}}^{\mu} < 0.15$, $E_{\mathrm{T}}^{\mathrm{topocone20}}/p_{\mathrm{T}}^{\mu} < 0.30$

Table 4.1: The seven isolation working points are described by their discriminating variables and defining criteria (12).

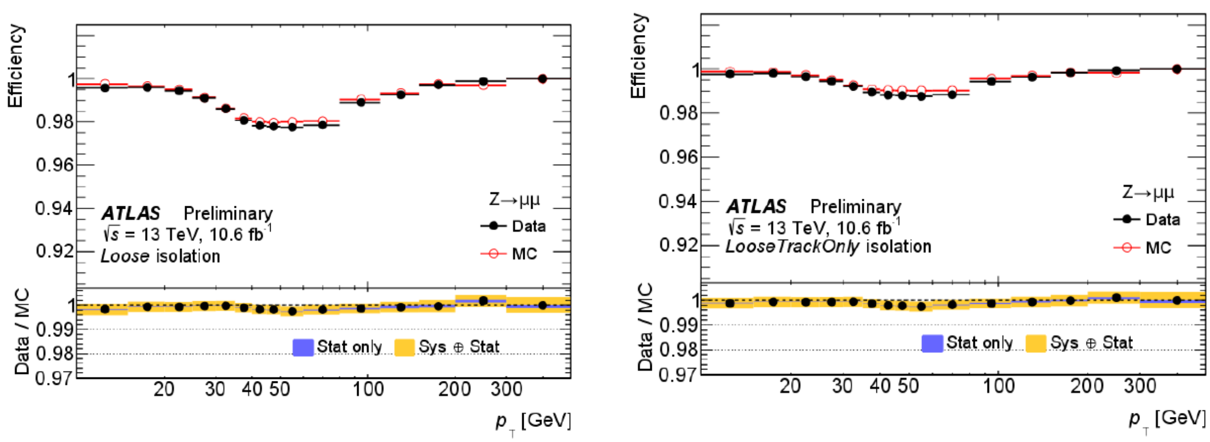

Figure 4.2: Isolation efficiency for the Loose (left) and LooseTrackOnly (right) muon isolation working points. The efficiency is displayed as a function of p_T in $Z \rightarrow \mu\mu$ events. The black markers show efficiency measured in data samples while the red show MC simulations. The bottom panel shows the ratio of the efficiency between the two as well as both statistical and systematic uncertainties (12).

simulated muon momentum. After applying the corrections we validate them by comparing the muon momentum scale and resolution between simulation and data over η, ϕ, and p_T.

I have been heavily involved in calculating the parameters that govern the muon momentum corrections and validating them with the newest datasets. Within the next section, I will describe muon momentum corrections and the parametrizations that define them.

We extract the calibration parameters with the transverse momentum of the ID and MS components of a CB track. The corrected transverse momentum is described by the following equation:

$$p_T^{\text{Cor,Det}} = \frac{p_T^{\text{MC,Det}} + \sum_{n=0}^{1} s_n^{\text{Det}}(\eta,\phi)(p_T^{\text{MC,Det}})^n}{1 + \sum_{m=0}^{2} \Delta r_m^{\text{Det}}(\eta,\phi)(p_T^{\text{MC,Det}})^{m-1} g_m}.$$

Here the g_m terms are normally distributed random variables with zero mean and unit width. The Δr and s terms describe momentum resolution smearing and scale corrections applied in specific detector regions, respectively. Both the ID and MS are divided into 18 pseudorapidity regions and the MS is divided into two ϕ bins separating the large and small sectors. Each of these bins leverages different alignment techniques and has different material distributions.

There are two s terms that represent different types of corrections. s_1 corrects for inaccuracy in the description of the magnetic field integral and the detector in the direction perpendicular to the magnetic field. s_0 corrects for the inaccuracy in the simulation of energy loss in the calorimeter and other materials. Since this loss is negligible in the ID, it is only nonzero in the MS (12).

The denominator introduces momentum smearing which broadens the p_T resolution in simulation. The parametrization of the smearing is defined:

$$\frac{\sigma(p_T)}{p_T} = r_0/p_T \oplus r_1 \oplus r_2 \cdot p_T.$$

In this equation r_0 is related to the fluctuations in energy loss in the traversed material, r_1 accounts for multiple scattering, local magnetic field inhomogeneities, and local radial displacements of hits, and r_2 describes intrinsic resolution effects caused by the spatial resolution of the hit measurements and by residual misalignment of the MS (12).

Correction parameters are extracted from data using a binned maximum-likelihood fit with templates derived from simulation which compares the invariant mass distributions for J/ψ and Z decay candidates in data and simulation. The muons are carefully selected to be compatible with tracks that start at the interaction point and penetrate both the ID and the MS. Muons are also selected to pass specific momentum and isolation criteria. The dimuon mass distribution of these tracks in data is fitted using a Crystal Ball function convoluted with an exponential background distribution in the ID and MS fits. The background model and its normalization are then used in the template fit. The fits are performed in $\eta - \phi$ regions of fit (ROFs) which compromise regions with uniform features in the ID and MS (12).

From these fits, we can find the smearing terms across all η regions. Once the corrections are applied we can validate that the agreement between data and MC is excellent. This is shown in Figure 4.3. r_0 is set to zero across all η regions since energy loss is negligible in the ID. r_1 and r_2 increase as η increases since spatial resolution decreases and inhomogeneities increase as as we move from the barrel to end-cap regions of both the ID and MS.

We must continue to study muon momentum corrections during ATLAS runs to validate muon calibration performance and account for discrepancies.

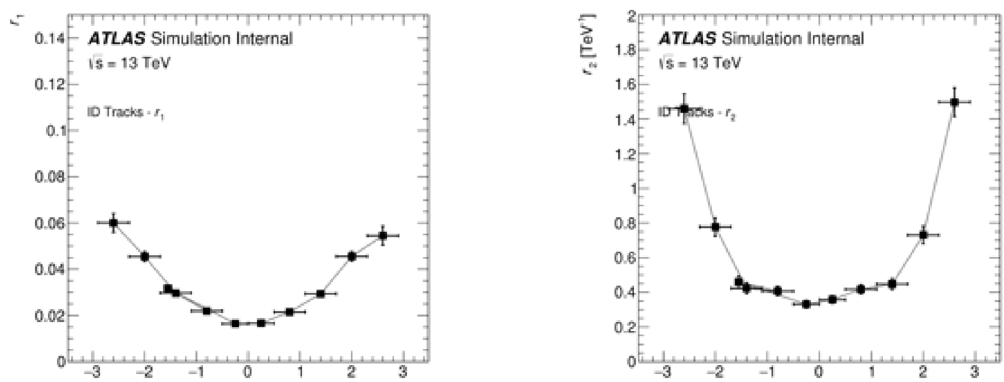

Figure 4.3: The r- values from each of 10 fits of resolution to p_T for ID muon simulations are shown. Each value corresponds to a particular ROF or η region. These plots show r_1 (left) and r_2 (right) as functions of leading muon η.

Chapter 5

Event Selection

5.1 Data and Monte Carlo samples

5.2 Object definitions

5.3 Event selection

Chapter 6

Backgrounds and Systematics

6.1 Backgrounds

6.2 Systematic uncertainties

Chapter 7

Results

7.1 Statistical analysis

7.2 Unfolding

7.3 Results and ratio measurements

Chapter 8

Conclusions

Place your conclusion here.

Bibliography

[det]

[old]

[3] (2010). Performance of the ATLAS Silicon Pattern Recognition Algorithm in Data and Simulation at $\sqrt{s} = 7$ TeV. Technical Report ATLAS-CONF-2010-072, CERN, Geneva.

[4] (2012). Radiofrequency cavities.

[5] (2019). Search for squarks and gluinos in final states with jets and missing transverse momentum using 139 fb^{-1} of $\sqrt{s}$ =13 TeV pp collision data with the ATLAS detector. Technical Report ATLAS-CONF-2019-040, CERN, Geneva.

[6] Aaboud, M., Aad, G., Abbott, B., Abdinov, O., Abeloos, B., Abhayasinghe, D., Abidi, S., AbouZeid, O., Abraham, N., Abramowicz, H., and et al. (2019a). Cross-section measurements of the higgs boson decaying into a pair of τ-leptons in proton-proton collisions at $\sqrt(s)$=13 tev with the atlas detector. *Physical Review D*, 99(7).

[7] Aaboud, M., Aad, G., Abbott, B., Abdinov, O., Abeloos, B., Abhayasinghe, D., Abidi, S., AbouZeid, O., Abraham, N., Abramowicz, H., and et al. (2019b). Measurements of gluon–gluon fusion and vector-boson fusion higgs boson production cross-sections in the

$h \rightarrow ww^* \rightarrow e\nu\mu\nu$ decay channel in *pp* collisions at $\sqrt(s)$=13tev with the atlas detector. *Physics Letters B*, 789:508–529.

[8] Aaboud, M., Aad, G., Abbott, B., Abdinov, O., Abeloos, B., Abidi, S., AbouZeid, O., Abraham, N., Abramowicz, H., Abreu, H., and et al. (2018a). Measurements of higgs boson properties in the diphoton decay channel with 36 fb^{-1} of *pp* collision data at $\sqrt{s} = 13\,\mathrm{tev}$ with the atlas detector. *Physical Review D*, 98(5).

[9] Aaboud, M., Aad, G., Abbott, B., Abdinov, O., Abeloos, B., Abidi, S. H., AbouZeid, O. S., Abraham, N. L., Abramowicz, H., and et al. (2018b). Measurement of the higgs boson coupling properties in the h $\rightarrow$ zz* $\rightarrow 4\ell$ decay channel at $\sqrt{s} = 13$ tev with the atlas detector. *Journal of High Energy Physics*, 2018(3).

[10] Aad, G., Abbott, B., Abdallah, J., Abdel Khalek, S., Abdinov, O., Aben, R., Abi, B., Abidi, S., Abolins, M., AbouZeid, O., and et al. (2014). Measurement of the higgs boson mass from the $h \rightarrow \gamma\gamma$ and $h \rightarrow zz^* \rightarrow 4\ell$ channels in *pp* collisions at center-of-mass energies of 7 and 8 tev with the atlas detector. *Physical Review D*, 90(5).

[11] Aad, G., Abbott, B., Abdallah, J., Abdelalim, A. A., Abdesselam, A., Abdinov, O., Abi, B., Abolins, M., Abramowicz, H., and et al. (2013). Jet energy measurement with the atlas detector in proton-proton collisions at $\sqrt{\mathrm{s}} = 7$ TeV. *The European Physical Journal C*, 73(3).

[12] Aad, G., Abbott, B., Abdallah, J., Abdinov, O., Abeloos, B., Aben, R., Abolins, M., AbouZeid, O. S., Abraham, N. L., and et al. (2016). Muon reconstruction performance of the atlas detector in proton–proton collision data at

$$\sqrt{s}$$

s =13 tev. *The European Physical Journal C*, 76(5).

[13] Benedikt, M., Collier, P., Mertens, V., Poole, J., and Schindl, K. (2004). LHC Design Report. 3. The LHC injector chain.

[14] Butterworth, J. M., Dissertori, G., and Salam, G. P. (2012). Hard Processes in Proton-Proton Collisions at the Large Hadron Collider. *Ann. Rev. Nucl. Part. Sci.*, 62:387–405.

[15] Campbell, J. M., Huston, J. W., and Stirling, W. J. (2007). Hard Interactions of Quarks and Gluons: A Primer for LHC Physics. *Rept. Prog. Phys.*, 70:89.

[16] CERN (2019). A new schedule for the lhc and its successor.

[17] Collaboration, A. (2017). Technical Design Report for the ATLAS Inner Tracker Strip Detector. Technical Report CERN-LHCC-2017-005. ATLAS-TDR-025, CERN, Geneva.

[18] Ellis, J. (2013). Higgs Physics. (KCL-PH-TH-2013-49. KCL-PH-TH-2013-49. LCTS-2013-36. CERN-PH-TH-2013-315):117–168. 52 p. 52 pages, 45 figures, Lectures presented at the ESHEP 2013 School of High-Energy Physics, to appear as part of the proceedings in a CERN Yellow Report.

[19] Evans, L. (2007). The large hadron collider. *New Journal of Physics*, 9(9):335–335.

[20] Halzen, F. and Martin, A. (1984). *Quarks and Leptons: An Introductory Course in Modern Particle Physics*.

[21] Illingworth, J. and Kittler, J. (1988). A survey of the hough transform. *Computer Vision, Graphics, and Image Processing*, 44(1):87 – 116.

[22] Rossi, L. (2010). Superconductivity: Its Role, Its Success and Its Setbacks in the Large Hadron Collider of CERN. *Supercond. Sci. Technol.*, 23(CERN-ATS-2010-006):034001. 27 p.

[23] Steerenberg, R. (2018). Lhc report: Protons: mission accomplished.

[24] Stirling, W. (2018). Private Communication...

[25] Tanabashi, M., Hagiwara, K., Hikasa, K., Nakamura, K., Sumino, Y., Takahashi, F., Tanaka, J., Agashe, K., Aielli, G., Amsler, C., Antonelli, M., Asner, D. M., Baer, H., Banerjee, S., Barnett, R. M., Basaglia, T., Bauer, C. W., Beatty, J. J., Belousov, V. I., Beringer, J., Bethke, S., Bettini, A., Bichsel, H., Biebel, O., Black, K. M., Blucher, E., Buchmuller, O., Burkert, V., Bychkov, M. A., Cahn, R. N., Carena, M., Ceccucci, A., Cerri, A., Chakraborty, D., Chen, M.-C., Chivukula, R. S., Cowan, G., Dahl, O., D'Ambrosio, G., Damour, T., de Florian, D., de Gouvêa, A., DeGrand, T., de Jong, P., Dissertori, G., Dobrescu, B. A., D'Onofrio, M., Doser, M., Drees, M., Dreiner, H. K., Dwyer, D. A., Eerola, P., Eidelman, S., Ellis, J., Erler, J., Ezhela, V. V., Fetscher, W., Fields, B. D., Firestone, R., Foster, B., Freitas, A., Gallagher, H., Garren, L., Gerber, H.-J., Gerbier, G., Gershon, T., Gershtein, Y., Gherghetta, T., Godizov, A. A., Goodman, M., Grab, C., Gritsan, A. V., Grojean, C., Groom, D. E., Grünewald, M., Gurtu, A., Gutsche, T., Haber, H. E., Hanhart, C., Hashimoto, S., Hayato, Y., Hayes, K. G., Hebecker, A., Heinemeyer, S., Heltsley, B., Hernández-Rey, J. J., Hisano, J., Höcker, A., Holder, J., Holtkamp, A., Hyodo, T., Irwin, K. D., Johnson, K. F., Kado, M., Karliner, M., Katz, U. F., Klein, S. R., Klempt, E., Kowalewski, R. V., Krauss, F., Kreps, M., Krusche, B., Kuyanov, Y. V., Kwon, Y., Lahav, O., Laiho, J., Lesgourgues, J., Liddle, A., Ligeti, Z., Lin, C.-J., Lippmann, C., Liss, T. M., Littenberg, L., Lugovsky, K. S., Lugovsky, S. B., Lusiani, A., Makida, Y., Maltoni, F., Mannel, T., Manohar, A. V., Marciano,

W. J., Martin, A. D., Masoni, A., Matthews, J., Meißner, U.-G., Milstead, D., Mitchell, R. E., Mönig, K., Molaro, P., Moortgat, F., Moskovic, M., Murayama, H., Narain, M., Nason, P., Navas, S., Neubert, M., Nevski, P., Nir, Y., Olive, K. A., Pagan Griso, S., Parsons, J., Patrignani, C., Peacock, J. A., Pennington, M., Petcov, S. T., Petrov, V. A., Pianori, E., Piepke, A., Pomarol, A., Quadt, A., Rademacker, J., Raffelt, G., Ratcliff, B. N., Richardson, P., Ringwald, A., Roesler, S., Rolli, S., Romaniouk, A., Rosenberg, L. J., Rosner, J. L., Rybka, G., Ryutin, R. A., Sachrajda, C. T., Sakai, Y., Salam, G. P., Sarkar, S., Sauli, F., Schneider, O., Scholberg, K., Schwartz, A. J., Scott, D., Sharma, V., Sharpe, S. R., Shutt, T., Silari, M., Sjöstrand, T., Skands, P., Skwarnicki, T., Smith, J. G., Smoot, G. F., Spanier, S., Spieler, H., Spiering, C., Stahl, A., Stone, S. L., Sumiyoshi, T., Syphers, M. J., Terashi, K., Terning, J., Thoma, U., Thorne, R. S., Tiator, L., Titov, M., Tkachenko, N. P., Törnqvist, N. A., Tovey, D. R., Valencia, G., Van de Water, R., Varelas, N., Venanzoni, G., Verde, L., Vincter, M. G., Vogel, P., Vogt, A., Wakely, S. P., Walkowiak, W., Walter, C. W., Wands, D., Ward, D. R., Wascko, M. O., Weiglein, G., Weinberg, D. H., Weinberg, E. J., White, M., Wiencke, L. R., Willocq, S., Wohl, C. G., Womersley, J., Woody, C. L., Workman, R. L., Yao, W.-M., Zeller, G. P., Zenin, O. V., Zhu, R.-Y., Zhu, S.-L., Zimmermann, F., Zyla, P. A., Anderson, J., Fuller, L., Lugovsky, V. S., and Schaffner, P. (2018). Review of particle physics. *Phys. Rev. D*, 98:030001.